PCCP

Evaluation of the Pr + O → PrO^+ + e^- Chemi-ionization Reaction Enthalpy and Praseodymium Oxide, Carbide, Dioxide, and Carbonyl Cation Bond Energies

Journal:	*Physical Chemistry Chemical Physics*
Manuscript ID	CP-ART-12-2020-006252.R1
Article Type:	Paper
Date Submitted by the Author:	04-Jan-2021
Complete List of Authors:	Ghiassee, Maryam ; University of Utah, Chemistry Stevenson, Brandon; University of Utah, Chemistry Armentrout, Peter; University of Utah, Chemistry

Submitted to Phys. Chem. Chem. Phys.

Evaluation of the Pr + O → PrO^+ + e^- Chemi-ionization Reaction Enthalpy and Praseodymium Oxide, Carbide, Dioxide, and Carbonyl Cation Bond Energies

Maryam Ghiassee, Brandon C. Stevenson, and P.B. Armentrout*

Department of Chemistry, University of Utah, Salt Lake City, Utah 84112

*Corresponding author. E-mail: armentrout@chem.utah.edu; ORCID: 0000-0003-2953-6039

ABSTRACT

Guided ion beam tandem mass spectrometry (GIBMS) was used to measure the kinetic energy dependent product ion cross sections for reactions of the lanthanide metal praseodymium cation (Pr^+) with O_2, CO_2, and CO and reactions of PrO^+ with CO, O_2, and Xe. PrO^+ is formed through barrierless exothermic processes when the atomic metal cation reacts with O_2 and CO_2, whereas all other reactions are observed to be endothermic. Analyses of the kinetic energy dependences of these cross sections yield 0 K bond dissociation energies (BDEs) for PrO^+, PrC^+, $PrCO^+$, and PrO_2^+. The 0 K BDE for PrO^+ is determined to be 7.62 ± 0.09 eV from the weighted average of five independent thresholds. This value is combined with the well-established ionization energy (IE) of Pr to indicate an exothermicity of the chemi-ionization reaction, Pr + O → PrO^+ + e^-, of 2.15 ± 0.09 eV. Additionally, BDEs of Pr^+-C, OPr^+-O, and Pr^+-CO are determined to be 2.97 ± 0.10. 2.47 ± 0.11, and 0.31 ± 0.07 eV. Theoretical Pr^+-O, Pr^+-C, OPr^+-O, and Pr^+-CO BDEs are calculated for comparison with experimental values. The Pr^+-O BDE is underestimated at the B3LYP and PBE0 level of theory but better agreement is obtained using the coupled-cluster with single, double, and perturbative triple excitations, CCSD(T), level. Density functional theory approaches yield better agreement for the BDEs of Pr^+-C, OPr^+-O, and Pr^+-CO.

INTRODUCTION

Natural fluctuations in electron density in the ionosphere can cause scintillation, the disruption of radio-wave transmission used in satellite communications. The Air Force is interested in mediating scintillation by using metal atoms that can react readily with oxygen atoms in the ionosphere via reaction (1).[1-3]

$$M + O \rightarrow MO^+ + e^- \quad (1)$$

This chemi-ionization reaction is one potential means to create a localized enhanced plasma in the ionosphere, which may mitigate naturally occurring ionospheric scintillation. Previous studies have shown that reaction (1) is exothermic for many lanthanide metals and a few transition and actinide metals, and that for these metals, the reverse recombination process can only occur by much slower three-body channels.[4] These elements form monoxides with ionization energies (IEs) smaller than their bond dissociation energies (BDEs). This property results in an exothermic release of an electron at thermal energies, as shown in Fig. 1. Atmospheric release experiments have been previously performed for the lanthanides samarium (Sm) and neodymium (Nd), and it was assumed that Sm underwent chemi-ionization while Nd did not.[5] However, this is inconsistent with the known thermochemistry for these metals, which indicates that the chemi-ionization reaction (1) is significantly more exothermic for Nd (1.76 ± 0.10 eV) than Sm (0.08 ± 0.07 eV).[4-8] Further, a recent study of the rate constants for the chemi-ionization reactions (1) of Sm and Nd, measured using a flow tube apparatus, indicated that Nd chemi-ionizes with O with high efficiency, while Sm does not.[5] One possible explanation for the atmospheric release experiments is misinterpretation because the green photoluminescence observed for Nd release was taken as a failure to see reaction (1).[5]

Recently,[7] the exothermicity of the Sm chemi-ionization reaction (1), $\Delta_{CI}H°_0(Sm)$, was determined indirectly through the thermodynamic cycles shown in Fig. 1. Guided ion beam tandem mass spectrometry (GIBMS) was used to measure $D_0(SmO^+)$ as $5.72_5 \pm 0.07$ eV. Using the second thermodynamic cycle, this BDE was combined with IE (Sm) = 5.6437 eV[9] to obtain an exothermicity of 0.08 ± 0.07 eV. This value was consistent with a less precise value of 0.14 ±

0.17 eV obtained independently from a remeasurement of IE(SmO) combined with literature D_0(SmO) in the first thermodynamic cycle.[7] These results indicate that the exothermicity of reaction (1) with Sm is ~0.2 eV lower than previous literature data, making it barely exothermic, which explained the smaller than expected magnitude for plasma enhancement observed in the Sm atmospheric release experiments.[1-3, 7] Additionally, GIBMS studies have also reevaluated the thermochemistry of the chemi-ionization reaction (1) with Gd and Nd, indicating that this process is exothermic by 1.54 ± 0.10 eV and 1.76 ± 0.10 eV, respectively.[8, 10]

In the present work, we extend these GIBMS studies to examine oxidation of the lanthanide praseodymium, Pr. The recent flow tube studies show that the chemi-ionization reaction of Pr with atomic O occurs with an efficiency of ~40% of the calculated hard sphere collision limit over the temperature range of 200 to 450 K.[11] An explanation for why reaction (1) with Pr is less efficient than several other lanthanides remained elusive but relied on literature thermochemistry, which is therefore reevaluated in the present work. Because IE(Pr) (5.463 ± 0.002 eV)[12, 13] is well-established, the exothermicity of the title reaction can be determined using thermodynamic cycle 2 in Fig. 1 if an accurate and precise value for $D_0(PrO^+)$ can be measured. Here, the BDE of PrO^+ is determined using GIBMS,[14, 15] which has been used in previous studies to obtain reliable diatomic metal oxide cation BDEs.[7, 8, 10, 16-28] In addition, the BDEs for PrC^+, PrO_2^+, and $PrCO^+$ at 0 K are determined from these experiments. Theoretical BDEs are additionally calculated for all four product ions and compared with the experimental BDEs.

Review of the literature thermochemistry

Using the thermodynamic cycle presented in Figure 1 and previously reported IE and BDE values, the chemi-ionization exothermicity for Pr can be determined. Probably the most precise available value for IE(PrO), 4.90 ± 0.10 eV, comes from extrapolating the linear portion of the ionization efficiency curve in electron ionization measurements by Ackermann, Rauh, and Thorn.[29] Additionally, rough measurements of 4.5 ± 0.5 eV,[30] 4.9 ± 0.5 eV,[31] as well as 5.02 ± 0.12 eV[32] (as reported by Cockett et al.[33]) are also available. Several recent studies have found

that IEs for other metal oxides taken from the study of Ackermann et al. are unreliable and can differ by up to ~0.8 eV from more recent measurements.[7, 10, 23, 28]

Previously reported PrO BDEs come from several sources and comparisons suffer from changes to the enthalpy and free energy functions used to extrapolate high temperature data to 0 K values. White and co-workers first examined the oxygen atom exchange reaction (2) between Pr and both M = La and Nd.[34] Ames et al. later included data for M = Tb and reanalyzed the previous data to report a 2nd law BDE for PrO at 0 K of 7.75 eV and a 3rd law value of 8.01 eV (averages of Tb and La results), for an average value of 7.88 ± 0.2 eV.[35]

$$Pr\ (g) + MO\ (g) \rightarrow PrO\ (g) + M\ (g) \qquad (2)$$

Brewer and Rosenblatt reevaluated these data choosing instead to average results relative to La and Nd (partly because the Tb results were lower by about 0.25 eV) for a recommended 0 K BDE of 7.76 ± 0.35 eV.[36] Fries and Cater then measured the enthalpy of reaction (2) with M = Y and report D_0 (PrO) = 7.78 ± 0.17 eV.[37]

Murad studied reaction (2) with Ti, obtaining D_0(PrO) = 7.63 ± 0.13 eV, and reevaluated the data of Ames et al. to obtain 7.74 ± 0.22 eV.[30] Cockett et al.[33] evaluated all the available data and recommended a BDE of 7.6 ± 0.1 eV, whereas the review of Pedley and Marshall[38] examined the previous measurements and proposed a value of 7.70 ± 0.17 eV, taken primarily from the M = Ti equilibrium results of Murad and the M = La equilibrium results of Ames et al., but the M = Nd and Tb results gave consistent results. Their evaluation of reaction (2) results for M = Y from Fries and Cater yielded a substantially higher value (7.88 ± 0.19 eV). Dulick, Murad, and Barrow reexamined the results of Murad for reaction (2) with Ti, suggesting D_0(PrO) = 7.74 ± 0.13 eV.[39] The review by Konings et al.[6] suggests a similar D_0(PrO) = 7.74 ± 0.08 eV on the basis of exchange reactions (2) from reevaluated work done by Walsh et al. (M = La), Murad (M = Ti), along with that of Fries and Cater (M = Y).[30, 34, 37]

Combining these various literature values for the PrO BDE (7.88 ± 0.2, 7.63 ± 0.13, 7.6 ± 0.1, 7.70 ± 0.17, 7.74 ± 0.08 eV) and IE(PrO) (4.90 ± 0.10 eV) using thermodynamic cycle 1 in

Fig. 1 gives the possible exothermicities for the Pr chemi-ionization reaction of 2.98 ± 0.22, 2.73 ± 0.16, 2.70 ± 0.14, 2.80 ± 0.20, 2.84 ± 0.13 eV, a range of 2.56 – 3.20 eV.

Alternatively, the thermodynamic cycles of Fig. 1 can be used to determine the BDE of PrO^+, using the BDEs and IE of PrO and IE(Pr). Ackermann, Rauh, and Thorn[29] reported $D_0(PrO^+)$ as 8.23 ± 0.10 eV using IE(Pr) and D_0(PrO) values from Brewer and Rosenblatt (5.37 ± 0.10 and 7.76 ± 0.10 eV, respectively).[36] Murad and Hildenbrand[40] reported a value of 8.20 ± 0.16 eV, using their D_0(PrO) value of 7.63 ± 0.13 eV. Schofield reported a $D_0(PrO^+)$ value of 8.31 eV (the origin of which is not provided).[4] Using the BDE (7.6 ± 0.1 eV) and IE (4.9 ± 0.2 eV) for PrO recommended by Cockett et al.,[33] Schwarz and co-workers[41] reported $D_0(PrO^+)$ = 8.20 ± 0.30 eV. Given the information reviewed above, we suggest a conservative PrO^+ BDE of 8.27 ± 0.20 eV, as determined using D_0(PrO) = 7.70 ± 0.17 eV,[38] IE(PrO) = 4.90 ± 0.1 eV,[29] and IE(Pr) = 5.4702 eV.[12, 13] If D_0(PrO) from Konigs et al.[6] is used instead, $D_0(PrO^+)$ = 8.31 ± 0.13 eV is obtained.

No experimental information regarding PrO_2 is available except for a rough ionization energy of 9.6 ± 0.5 eV and a heat of reaction at 2000 K for $PrO_2 \rightarrow PrO + ½ O_2$ of 1.74 ± 0.14 eV from Staley and Norman.[31] Kordis and Gingerich[42] estimated that $D_0(PrO_2)$ = 14.66 ± 0.95 eV (atomization energy), which would correspond to D_0(OPr-O) = 6.96 ± 0.97 eV given D_0(PrO) = 7.70 ± 0.17 eV. Coupling this value with IE(PrO) = 4.9 ± 0.1 eV and $IE(PrO_2)$ = 9.6 ± 0.5 eV, suggests that $D_0(OPr^+\text{-}O)$ = 2.26 ± 1.10 eV.

EXPERIMENTAL AND THEORETICAL METHODS

GIBMS

The guided ion beam tandem mass spectrometer and experimental procedure used in this study have been described in detail elsewhere.[14, 15, 43] Briefly, Pr^+ ions were created using a direct-current discharge flow tube (DC/FT) ion source.[44] A dc voltage of -1000 – -1400 V was applied to a cathode consisting of Pr foil (Alpha Aesar, Haverhill, MA) mounted to an iron holder. A gas mixture of approximately 10% argon and 90% helium was continuously introduced

into the source at a pressure of ~ 0.4 Torr. Ar cations produced in the discharge were accelerated into the Pr foil and sputtered singly charged Pr^+, which were swept into a 1 m long flow tube, where they underwent ~10^5 thermalizing collisions with the He and Ar carrier gasses. PrO^+ ions were generated by introducing O_2 gas to the flow tube ~15 cm downstream from the ion source. On the basis of previous characterization of metal ions formed in the DC/FT ion source, the Pr ions are assumed to have an effective electronic state distribution characterized by a temperature between 300 and 1100 K.[45-47] As previously detailed,[48] this corresponds to an average electronic energy (E_{el}) for Pr^+ of $0.03_6 \pm 0.02_9$ eV and was taken into account when determining 0 K threshold energies from modeling the data, as described below.

Reactant ions were skimmed, focused, and mass selected using a magnetic momentum analyzer, where ^{141}Pr (the only stable isotope) was selected. The precursor ions were then decelerated to a desired kinetic energy prior to entering a radio frequency (rf) octopole ion beam guide.[14, 49, 50] Part of the octopole is surrounded by a reaction cell in which neutral reactant gases (O_2, CO_2, CO, or Xe) were introduced at pressures ranging from 0.1 to 0.3 mTorr. This pressure range is sufficiently low to ensure that single collisions predominantly occurred between the precursor ions and neutral gases. This was confirmed by verifying that the cross sections did not depend on pressure. Precursor and product ions drifted to the end of the octopole where they were mass analyzed using a quadrupole mass filter, and their intensities were then measured using a Daly detector.[51] As previously described,[49] product ion intensities were converted to reaction cross sections after correction for signal noise and any background reactions that did not occur in the reaction cell. Uncertainties in the absolute cross sections are estimated as ±20%.[49] Laboratory ion energies (lab) were converted to the center-of-mass (CM) frame using the equation $E_{CM} = E_{lab} \times m / (m + M)$, where m is the mass of the neutral reactant and M is the mass of the reactant ion. Retarding measurements were used to determine the kinetic energy distribution,[49] which had a typical full-width at half-maximum (fwhm) of 0.4 – 0.6 eV (lab), and the zero of the absolute energy, which had an uncertainty of ± 0.1 eV (lab).

Data Analysis

The kinetic energy dependent cross sections of endothermic reactions were modeled using eqn (3).

$$\sigma(E) = \sigma_0 \sum g_i (E + E_i + E_{el} - E_0)^n/E \quad (3)$$

Here, E is the relative kinetic energy of the reactants, σ_0 is an empirical scaling factor, n is an adjustable parameter (which describes the energy deposition efficiency in collision-induced dissociation[52]), E_i is the internal energy of the reactants' vibrational and rotational states having populations g_i ($\sum g_i = 1$), E_{el} is the average electronic energy of Pr^+ (defined above), and E_0 is the 0 K threshold energy. Prior to comparison to the experimental cross sections, eqn (3) was convolved over the kinetic energy distribution of the reactants. Optimized values of the parameters σ_0, n, and E_0 were obtained using a nonlinear least-squares method to best reproduce the experimental cross sections. Uncertainties in E_0 were calculated from the threshold values for at least four independent data sets over a range of n values combined with the absolute uncertainties in the kinetic energy scale and internal energies of the reactant ions. For exchange reactions, $Pr^+ + RL \rightarrow PrR^+ + L$, the experimentally measured threshold energies were used to determine BDEs, $D_0(Pr^+\text{-}R)$, using eqn (4).

$$D_0(Pr^+\text{-}R) = D_0(R\text{-}L) - E_0 \quad (4)$$

This equation relies on the assumption that there are no barriers in excess of the endothermicity of the reaction, which is often the case for ion-neutral interactions.[53] $D_0(R\text{-}L)$ values for the neutral reactants were taken from data in the NIST webBook.[54] For collision-induced dissociation (CID) experiments at collision energies near threshold, the mechanism of reaction is expected to be transfer of collisional energy into vibrational excitation. Thus, as shown in many previous studies from our laboratory including those for diatomic metal oxide cations,[7, 8, 10, 14, 16, 23, 55-57] the measured E_0 values correspond directly to the desired BDE, here $D_0(Pr^+\text{-}O)$. This conclusion is further demonstrated by the good agreement obtained between CID thresholds and BDEs obtained from exchange reactions, as detailed below.

In the exchange reactions, the cross section for the PrR^+ products peak at an energy near D_0(R-L) because this is the thermodynamic onset for dissociation of the product to Pr^+ and R. Dissociation at higher energies was accounted for using a statistical model outlined elsewhere[58] that depends on two parameters: *p*, similar to *n* but holding only integral values, and E_D, which designates the energy onset for dissociation, generally D_0(R-L).

Quantum chemical calculations

Theoretical calculations were performed using the Gaussian 16 suite of programs.[59] Ground and low-energy states and BDEs of PrO^+, PrC^+, PrO_2^+, and $PrCO^+$ were calculated using B3LYP,[60, 61] PBE0,[62, 63] and coupled-cluster with single, double, and perturbative triple excitations, CCSD(T),[64-67] levels of theory. These calculations utilized the 6-311+G(3df) Pople basis set for O and C and the atomic natural orbital[68] (ANO) (14s13p10d8f6g)/ [6s6p5p4f3g] and the segmented[69] Stuttgart Dresden (Seg. SDD) (14s13p10d8f6g)/ [10s8p5d4f3g] basis sets for Pr. Both basis sets for Pr use the Stuttgart Dresden relativistic effective small core (28 electron) potential.[70] Additionally, BDEs for the PrO^+, PrC^+, PrO_2^+, and $PrCO^+$ were calculated using the 2nd-order Douglas-Kroll-Hess Hamiltonian (DKH2)[71, 72] with the all electron cc-pVXZ-DK3 basis sets for Pr,[73] and the aug-cc-pVXZ-DK basis sets for O and C, where X = D, T and Q. CCSD(T) calculations using the ANO and Seg. SDD basis set for Pr included all explicit electrons in the correlation calculations (with the "full" keyword), whereas those using the all-electron basis sets include only the outer electrons of Pr in 4f, 5s, 5p, 5d and 6s orbitals (with the "window = 24" keyword). Extrapolation to the complete basis set (CBS) limit using single point energies calculated with cc-pVXZ-DK3 (X = D, T and Q) and the formula E[CBS] = 1.676755 E[Q] - 0.711622 E[T] + 0.0348867 E[D][74] was used to obtain additional theoretical BDEs for PrO^+ PrC^+, PrO_2^+, and $PrCO^+$. To determine the energies at the CCSD(T) level, single point calculations were conducted using geometries and vibrational frequencies optimized at the PBE0 level. All energies were zero-point energy corrected using frequencies scaled by 0.989.[75] The rotational constant (0.391 cm^{-1}) and the vibrational frequency (932 cm^{-1}) for PrO^+ used in

modeling of the experimental cross sections were obtained at the PBE0 level of theory and ANO basis set for Pr.

EXPERIMENTAL RESULTS

Pr^+ Reaction with O_2

Product ion cross sections for the reaction of Pr^+ and O_2 as a function of CM energy in the range 0.1 to 20 eV are shown in Fig. 2. Two products were formed in this reaction according to reactions (5) and (6).

$$Pr^+ + O_2 \rightarrow PrO^+ + O \quad (5)$$

$$PrO^+ + O_2 \rightarrow PrO_2^+ + O \quad (6)$$

PrO^+ is formed with a significant cross section (~100 $Å^2$) at the lowest collision energy (0.1 eV) and its cross section decreases with increasing collision energy. This behavior indicates that the PrO^+ product is formed through an exothermic and barrierless reaction. The black line in Fig. 2 corresponds to the theoretical collision limit expected from the Langevin-Gioumousis-Stevenson (LGS)[76] model that assumes an ion-induced dipole interaction. At low collision energies (<2 eV), the experimental PrO^+ cross section has an energy dependence of $E^{-0.54 \pm 0.05}$, comparable to that of the LGS cross section, but with a larger magnitude by 74 ± 35%. These experimental cross sections can be converted to a rate constant (k) as described previously.[49] The average experimental rate constant (k_5) for reaction (5) obtained for collision energies below 2 eV is (9.8 ± 2.0) × 10^{-10} cm^3/s, higher than the LGS rate constant (k_{LGS}) of 5.7 × 10^{-10} cm^3/s. The resulting reaction efficiency is 174 ± 35% where the uncertainty reflects the 20% absolute uncertainty in the measured cross sections. This result is sufficiently unusual that we verified it could be reproduced upon several separate occasions, that it is not the result of a pressure dependent phenomenon, and that cross sections for the well-characterized $Ar^+ + D_2 \rightarrow ArD^+ + D$ reaction[49] and the $Sm^+ + O_2 \rightarrow SmO^+ + O$ reaction[7] were reproduced. Similar deviations between experimental MO^+ cross section and σ_{LGS} at low energies have been previously observed in the reactions of M^+ = Zr^+, Nb^+, and Th^+ with O_2.[22, 28] A possible explanation for this observed

phenomenon has been previously explored in detail.[22] Briefly, these reactions may couple with the $M^{2+} + O_2^-$ asymptote, resulting in a Coulombic interaction that is more attractive than the ion-induced dipole interaction incorporated into the LGS model.

The present results are also higher than the rate constant of (4.3 ± 1.0) × 10^{-10} cm^3/s (reaction efficiency = 75 ± 23%) measured for Pr^+ reacting with O_2 at thermal (296 ± 2 K) energies and 0.35 Torr of He using a inductively coupled plasma/selected-ion flow tube (ICP/SIFT) apparatus.[77] This discrepancy could result from the differing ion sources (DC discharge vs. ICP) and collision conditions (single collision vs. high pressure bath gas), although we note that good agreement is obtained for the reaction of Pr^+ with CO_2, discussed below. Similar discrepancies have been noted for other lanthanide cations reacting with O_2, where GIBMS studies obtained reaction efficiencies at thermal energies of 93 ± 19% for Nd^+,[8] 100 ± 20% for Sm^+ and Gd^+,[7, 10] but 57 ± 17%, 48 ± 14%, and 86 ± 26%, respectively, for the ICP/SIFT measurements.[77] In the case of Sm^+, additional SIFT studies where the reactant ions were generated by electrospray ionization were also conducted and obtained a reaction efficiency of 49 ± 15%.[7] Interestingly, subsequent unpublished studies have revealed that this SIFT study included SmH^+ in the reactants, which lowered the observed reaction efficiency. These studies of the pure $Sm^+ + O_2$ reaction obtain a reaction efficiency within experimental uncertainty of the GIBMS result. Whether such problems might also plague the ICP/SIFT studies is completely speculative.

At collision energies above 2 eV, the PrO^+ cross section begins to decline more rapidly than the LGS model. This behavior has previously preen observed in other similar systems and is the result of angular momentum constraints.[8, 20, 78, 79] In reaction (5), the reduced mass of the products is about half that of the reactants, making it harder to conserve orbital angular momentum during the collision. Thus, the centrifugal barrier in the product channel increases more rapidly with energy than that in the reactant channel, until eventually the former exceeds the latter, decreasing the reaction efficiency. As detailed previously,[79] a simple model can predict at what energy this deviation between the experimental and LGS cross section can occur. Using

an exothermicity for reaction (5) of 2.50 ± 0.09 eV (determined from $D_0(Pr^+\text{-}O)$ = 7.62 ± 0.09 eV determined below and $D_0(O\text{-}O)$ = 5.117 eV), the model predicts that the product channel barrier should begin to dominate the formation of PrO^+ near 1.0 eV, consistent with the decline in the PrO^+ cross section shown in Fig 1. At still higher energies, the PrO^+ cross section levels from about 5 – 8 eV, before declining even more rapidly. The latter behavior indicates the PrO^+ product has sufficient energy to dissociate, a process that can begin at $D_0(O_2)$ = 5.117 eV. The observed behavior is more closely correlated with the spectator stripping (SS) model,[79] where the Pr^+ is assumed to interact with only one of the oxygen atoms with the other oxygen serving as a "spectator". The SS model predicts that dissociation of the PrO^+ product should begin at 9.3 eV.

In the reaction of Pr^+ with O_2, PrO_2^+ was also formed but with a relatively small cross sections that reaches a maximum of only 5.0 × 10^{-18} cm^2, Fig. 2. Formation of PrO_2^+ has an apparent threshold of ~1 eV and peaks near 3.0 eV. Additionally, the PrO_2^+ cross section is linearly dependent on the O_2 pressure, indicating that this product is formed through a sequential reaction of the abundant PrO^+ product ion with a second neutral reactant, process (6). This conclusion is confirmed by the direct examination of reaction (6), as described below.

Pr^+ Reaction with CO_2

The kinetic energy dependent cross sections for the reaction of Pr^+ and CO_2 are shown in Fig. 3. Pr^+ reacts with CO_2 to form PrO^+, PrO_2^+, and $PrCO^+$ according to reactions (7) - (9).

$$Pr^+ + CO_2 \rightarrow PrO^+ + CO \quad (7)$$

$$\rightarrow PrCO^+ + O \quad (8)$$

$$\rightarrow PrO_2^+ + C \quad (9)$$

None of the reactions exhibit any dependence on CO_2 pressure, which confirms that PrO_2^+ is not generated by a sequential reaction of the PrO^+ product, unlike reaction (6). Similar to reaction (5), PrO^+ is formed with a significant cross section at the lowest collision energy (45 $Å^2$ at 0.054 eV) and its cross section decreases with increasing collision energy. Once again, this indicates that PrO^+ is formed exothermically through a barrierless reaction. The average experimental rate

constant (k_7) for reaction (7) determined for collision energies below 0.3 eV is (1.6 ± 0.3) × 10^{-10} cm^3/s, smaller than the LGS rate constant (k_{LGS}) of 6.4 × 10^{-10} cm^3/s, for a reaction efficiency of 25 ± 5 %. These values are consistent with the experimental rate constant of (1.6 ± 0.5) × 10^{-10} cm^3/s (efficiency = 25 ± 8 %) observed at thermal (296 ± 2 K) energies and 0.35 Torr of He in ICP/SIFT experiments.[80]

The PrO^+ cross section declines with increasing kinetic energy as $E^{-0.6 \pm 0.2}$, comparable with the $E^{-1/2}$ dependence of the LGS collision model. It then levels from 0.5 to 2 eV and increases at higher energies, reaching a reaction efficiency near 85% by ~5.5 eV. These changes in the cross section suggest that a new channel for PrO^+ formation begins near 1 and/or 2 eV. As previously discussed,[8, 81-84] one explanation for such behavior involves conservation of electronic spin in reaction (7). Because both CO_2 and CO have singlet spin states, conservation of spin dictates that the PrO^+ product and Pr^+ reactant of reaction (7) must have the same spin state. In contrast, Pr^+ has a ^5I ground state, whereas the ground state of PrO^+ is ^3H according to the theoretical calculations below, such that formation of ground state PrO^+ does *not* conserve spin. This is one potential explanation for the inefficiency of reaction (7) at low energies.[85] The efficient but endothermic channel observed starting above ~1 or 2 eV may then correlate to a spin conserving reaction, a hypothesis that is explored computationally below.

In the reaction of Pr^+ with CO_2, the $PrCO^+$ product ion is additionally formed according reaction (8). The data in Fig. 3 indicate that reaction (8) is endothermic, with an apparent onset energy near 4 eV. The $PrCO^+$ cross section peaks at ~6 eV and decreases sharply at higher energies because once the system exceeds D_0(OC-O) = 5.4532 ± 0.0003 eV,[86] the product ion has enough energy to dissociate into Pr^+ and CO.

PrO_2^+ is formed according to reaction (9). Given D_0(OPr^+-O) = 2.47 ± 0.11 and D_0(Pr^+-O) = 7.62 ± 0.09 eV, as determined below, the threshold is expected to be 6.47 ± 0.14 eV with the PrO_2^+ having sufficient energy to dissociate at energies exceeding 8.94 ± 0.09 eV. These values are in relatively good agreement with the experimental data shown in Fig. 2.

Pr^+ Reaction with CO

Pr^+ reacts with CO to form PrO^+ and PrC^+ according to reactions (10) and (11).

$$Pr^+ + CO \rightarrow PrO^+ + C \quad (10)$$

$$\rightarrow PrC^+ + O \quad (11)$$

Product ion cross sections as a function of kinetic energy for these reactions are shown in Fig. 4. The PrO^+ cross section shown in Fig. 4 has been corrected for an exothermic tail resulting from an O_2 impurity of ~0.07%. Both reactions (10) and (11) are endothermic with apparent threshold energies of ~3 and ~8 eV, respectively. Both cross sections increase with collision energy, peak near $D_0(C\text{-}O) = 11.111 \pm 0.001$ eV,[87] and then decrease at higher energies because both product ions dissociate. The PrO^+ peaks at somewhat lower energies than $D_0(C\text{-}O)$, in large part because of competition with the PrC^+ channel.

CID of PrO^+ with Xe

CID of PrO^+ was performed with Xe to measure the BDE of PrO^+ directly according to reaction (12).

$$PrO^+ + Xe \rightarrow Pr^+ + O + Xe \quad (12)$$

Previous studies have indicated that more accurate BDEs can be obtained from CID reactions using Xe as the neutral collision gas.[10, 16, 23, 28] Here, Pr^+ is the only product ion observed and has a cross section with an apparent threshold of ~8 eV, as shown in Fig. 5.

PrO^+ Reaction with CO

Additional insight into the Pr^+ reaction with CO_2 to form PrO^+ and CO can be obtained by investigating the reverse of reaction (7). Because reaction (7) is clearly exothermic, the reverse reaction (13) must be endothermic.

$$PrO^+ + CO \rightarrow Pr^+ + CO_2 \quad (13)$$

Fig. 6 shows the product ion cross sections as a function of kinetic energy for the reaction between PrO^+ and CO. Two product ions, Pr^+ and PrO_2^+, are observed. The cross section for the formation of Pr^+ exhibits two features. The cross section rises slowly starting with an apparent

threshold energy near 3 eV, a process that must correspond to reaction (13). Starting near 8 eV, the cross section increases more rapidly, behavior that parallels that found for reaction (12), as shown in Fig. 5. This behavior is consistent with the formation of Pr^+ through the CID reaction (14).

$$PrO^+ + CO \rightarrow Pr^+ + O + CO \quad (14)$$

As shown in Fig. 6, PrO_2^+ is formed with an apparent onset near 8 eV, and its cross section increases with collision energy until it peaks at ~12 eV, somewhat above $D_0(CO)$. This product ion is formed according to the exchange reaction (15).

$$PrO^+ + CO \rightarrow PrO_2^+ + C \quad (15)$$

The shift in the peak to higher energy has been observed in previous studies of analogous reactions involving other metal oxide cations reacting with CO.[8, 10, 88] Such a shift could be the result of strong competition with the CID reaction or can be attributed to an impulsive reaction mechanism. The latter idea can be assessed by considering the spectator stripping (SS) model, where the PrO^+ is assumed to interact only with the oxygen atom of carbon monoxide while the carbon serves as a "spectator". As previously discussed,[89, 90] for endothermic processes, the SS model is modified such that a smaller fraction of available energy goes into translational energy. Using the value for $D_0(OPr^+\text{-}O)$ of 2.47 eV derived below, this modified endothermic stripping model predicts that the PrO_2^+ cross section should peak near 12.6 ± 0.2 eV, in qualitative agreement with experimental observation.

PrO^+ Reaction with O_2

The kinetic energy dependent cross sections for the reaction of PrO^+ with O_2 are shown in Fig. 7. Two product ions, PrO_2^+ and Pr^+, are formed according to reactions (16) and (17).

$$PrO^+ + O_2 \rightarrow PrO_2^+ + O \quad (16)$$

$$PrO^+ + O_2 \rightarrow Pr^+ + O_2 + O \quad (17)$$

The PrO_2^+ product is formed via the exchange reaction (16) with an apparent threshold energy of ~3 eV. The PrO_2^+ cross section increases and peaks near 6 eV where it then begins to decline at

higher energies. The second product, Pr^+, is formed through the CID reaction (17). This assignment is supported by the apparent threshold energy of ~ 8 eV, which is similar to the threshold energy for the Pr^+ product ion in the CID reaction of PrO^+ with Xe as the neutral collision gas, Fig. 5. Conceivably, Pr^+ could also be formed along with O_3 as the neutral, but the O_2-O bond is quite weak (1.062 eV)[87] such that this channel must have a small cross section.

BDEs from exchange reactions

The Pr^+ exchange reactions with O_2, reaction (5), and CO_2, reaction (7), form PrO^+ exothermically through barrierless processes. Thus, $D_0(Pr^+\text{-O})$ must exceed the BDEs of O_2 and OC-O, 5.117 and 5.453 eV, respectively.[86] In contrast, PrO^+ was formed endothermically when reacted with CO, reaction (10), indicating that $D_0(Pr^+\text{-O})$ must be less than $D_0(\text{C-O})$ = 11.111 eV.

The PrO^+ product ion cross section resulting from reaction (10) was modeled using eqn (3), as shown in Fig. 4. This yields a threshold energy of 3.60 ± 0.12 eV. Combining the E_0 value with $D_0(\text{C-O})$ using eqn (4) gives $D_0(Pr^+\text{-O})$ = 7.51 ± 0.12 eV. Optimized fitting parameters used in eqn (3) for all modeled endothermic reactions are summarized in Table 1. The reverse of reaction (7) was observed to form Pr^+ endothermically according to reaction (13). Modeling the low-energy feature in the Pr^+ cross section of Fig. 6 yields a 0 K threshold energy of 2.21 ± 0.22 eV, which can be combined with $D_0(\text{OC-O})$ to give $D_0(Pr^+\text{-O})$ = 7.66 ± 0.22 eV, in good agreement with the result from reaction (10).

In the reaction between Pr^+ and CO, an additional product is formed endothermically, PrC^+ in reaction (11). Modeling the product ion cross section using eqn (3), as shown in Fig. 4, results in a threshold energy of 8.14 ± 0.10 eV, which corresponds to $D_0(Pr^+\text{-C})$ = 2.97 ± 0.10 eV. Also, $PrCO^+$ is formed endothermically in the exchange reaction between Pr^+ and CO_2, reaction (8). Modeling the data, shown in Fig. 3, results in a threshold energy of 5.14 ± 0.07 eV, which combined with $D_0(\text{OC-O})$ gives $D_0(Pr^+\text{-CO})$ = 0.31 ± 0.07 eV.

The reactions of PrO^+ with CO, reaction (15), and O_2, reaction (16), form PrO_2^+ products endothermically. Using eqn (3), the PrO_2^+ cross section in reaction (15) was modeled to obtain a threshold energy of 8.59 ± 0.13 eV, which using eqn (4) gives $D_0(OPr^+\text{-}O)$ = 2.52 ± 0.13 eV. Similar modeling of the PrO_2^+ cross section in reaction (16) yields a threshold energy of 2.78 ± 0.22 eV. Using eqn (4) and $D_0(O_2)$ = 5.117 eV[87] gives $D_0(OPr^+\text{-}O)$ = 2.34 ± 0.22 eV, within experimental uncertainty of the results from reaction (15). The weighted average of these two results is taken as our best determination of the OPr^+-O bond energy, 2.47 ± 0.11 eV (where the uncertainty is one standard deviation of the mean). Next, we return to reaction (6), the sequential formation of PrO_2^+. Here the cross section for sequential reaction (6) does not match that from reaction (16), a result of the PrO^+ reactant for reaction (6) being formed exothermically in reaction (5). Using the final thermochemistry for PrO^+ determined below, reaction (6) is exothermic by 2.50 ± 0.08 eV. Assuming that all this exothermicity is available to the PrO^+ product, the threshold in reaction (6) shifts from 2.78 ± 0.22 eV to 0.28 ± 0.23 eV, and its dissociation onset shifts from 5.12 eV to 2.62 eV. This predicted threshold energy is slightly lower than the apparent experimental threshold, while the predicted dissociation onset matches well with the peak in the PrO_2^+ cross section in Fig. 2.

Lastly, the endothermic feature in the PrO^+ cross section in reaction (7) can be modeled using eqn (3) after subtracting a model of the exothermic feature. The remaining endothermic cross section exhibited two features corresponding to rough onsets of 1 and 2 eV. To accurately reproduce this behavior, two models of eqn (3) were required. The first utilized a threshold energy of 0.69 ± 0.12 eV with the second beginning at 2.35 ± 0.2 eV. Although such an interpretation is fairly speculative, the potential meanings of these values are discussed in more detail below.

BDEs from CID

Additional $D_0(Pr^+\text{-}O)$ values can be obtained from the CID reactions with Xe, O_2, and CO as the neutral collision gas. In these experiments, the PrO^+ dissociates when its internal energy is

greater than its BDE. Therefore, the E_0 values correspond directly to the 0 K BDE for PrO^+. The CID experiments with Xe and O_2 yield $D_0(Pr^+\text{-}O)$ of 7.58 ± 0.20 eV and 7.73 ± 0.13 eV, respectively, Table 1. For the CID reaction of PrO^+ with CO, if the lower energy feature is ignored, the higher energy feature can be modeled directly to obtain $D_0(Pr^+\text{-}O)$ = 7.72 ± 0.23 eV, which agrees well with the Xe and O_2 CID thresholds. This suggests that the Pr^+ cross section resulting from reaction (13) exhibits a sharp decline at energies above the onset for the CID process, as shown in Fig. 6. This behavior is similar to that observed for other lanthanide cations in analogous reactions.[8, 10] The rationale for such behavior is that the CID reaction (14) is entropically much more favorable than reaction (13), because of the much higher phase space associated with the additional three translational degrees of freedom available to the products of the CID process. Thus, when CID becomes available, it dominates the reactions observed.

The slightly higher threshold energies obtained in the CID reactions with CO and O_2 could be a result of less efficient collision energy transfer because, unlike Xe, CO and O_2 can carry away energy in vibrational and rotational modes. Further, this delay in the energy threshold could be the effect of the strength of the interaction of the PrO^+ ion with the neutral, because Xe (α = 4.02 Å^3) has a polarizability about a factor of 2 larger than that for O_2 (α = 1.57 Å^3) and CO (α = 1.94 Å^3).[91] This leads to a longer-lived collision allowing more complete energy transfer in the threshold region for the CID experiments with Xe.

BDEs from the CID reactions, 7.72 ± 0.23, 7.73 ± 0.13, and 7.58 ± 0.20 eV are consistent with each other and with values from the two exchange reactions (10) and (13), 7.51 ± 0.12 and 7.66 ± 0.22 eV, respectively, Table 1. A weighted average of all five values provides $D_0(Pr^+\text{-}O)$ = 7.62 ± 0.09 eV; however, for the reasons discussed in the previous paragraph, if the slightly higher BDEs obtained from the CID reactions of PrO^+ with O_2 and CO are omitted from the weighted average, $D_0(Pr^+\text{-}O)$ = 7.55 ± 0.09 eV is obtained. In both cases, the uncertainty is one standard deviation of the mean. We take the more conservative value of 7.62 ± 0.09 eV that includes all five measurements as our best determination.

THEORETICAL RESULTS

Theoretical calculations for Pr^+

Energies for the ground and low-lying excited states of Pr^+ were calculated using B3LYP, PBE0, and CCSD(T,full) levels of theory using the ANO and Seg. SDD basis sets to determine which basis sets and levels of theory provide reliable thermochemistry. Comparison of these energies with corresponding experimental energies (averaged over spin-orbit levels weighted by the 2J + 1 degeneracy for each level) is shown in Fig. 8 and summarized in Table S1 (ESI†). The experimental ground state for Pr^+ (^{5}I, $4f^36s^1$) is accurately identified at the B3LYP and PBE0 levels of theory with the ^{3}I ($4f^36s^1$) state lying only 0.05 – 0.09 eV higher, compared to the experimental value of 0.16 eV (averaged over spin-orbit levels). Theoretical calculations for the ^{5}L and ^{5}K excited states, having $4f^3(^5I)5d^1$ electronic configurations, give identical energies because the only difference between these states is the orbital angular momentum of the 5d electron orbital, as previously discussed.[8] Theory overestimates the ^{5}L and ^{5}K excited state energies by 0.13 – 0.31 eV. At the CCSD(T,full) levels of theory, the ^{5}I lies 0.002 – 0.003 eV above the ^{3}I state and the ^{5}L and ^{5}K excited state energies overestimate experiment by 0.32 eV.

Overall, the PBE levels of theory using both the ANO and Seg. SDD basis set provide the most reliable energy levels compared to the experimental values, suggesting it will provide reliable BDEs for PrO^+, PrC^+, PrO_2^+, and $PrCO^+$. A more detailed discussion of these theoretical calculations is available in the ESI†.

Ground states for PrO^+, PrC^+, PrO_2^+, $PrCO^+$

Theoretical calculations were performed to determine the ground and low-lying excited states of PrO^+, PrC^+, PrO_2^+, and $PrCO^+$, as discussed in and summarized by Tables S2 – S5 (ESI†), respectively. For PrO^+, the ground state was determined to be ^{3}H ($[\delta^1\phi^1]\,\pi^4\sigma^2$) at all levels of theory and basis sets, after spin-orbit (SO) corrections. In the ^{3}H state, valence electrons from 5d orbitals on Pr (2 electrons) and 2p orbitals on O (4 electrons) form σ and π bonds, resulting in a triple bond (Fig. 9). The remaining two valence electrons are non-bonding and

located in the 4f orbitals of Pr, designated using square brackets. Various occupations of the 4f orbitals by the two nonbonding electrons can lead to many low-lying excited electronic states in all these molecules. Low-lying triplet states having electronic configurations $^3\Gamma$ ($[\pi^1\phi^1]\ \pi^4\sigma^2$), $^3\Delta$ ($[\sigma^1\delta^1]\ \pi^4\sigma^2$), and $^3\Sigma$ ($[\delta^2]\ \pi^4\sigma^2$) lie 0.03 – 0.29, 0.31 – 0.73, and 0.48 – 0.78 eV above the ^{3}H ground state, respectively. PrO^+ quintet states require the promotion of a bonding electron to a 4f orbital and lie 2 – 4 eV above the ground state. These quintet states have bond lengths of 1.988 – 2.063 Å, more extended than the triplet state bond lengths of 1.733 – 1.759 Å. This increase in bond length correlates to the lower bond order in the quintet states.

For PrC^+, most calculations predicted the ground state to be ^{5}I ($[\delta^1\phi^1]\ \sigma^1\pi^3$). At the B3LYP/Seg.SDD level of theory, the ground state was determined to be ^{5}H ($[\pi^1\phi^1]\ \sigma^1\pi^3$) with the ^{5}I state lying 0.04 eV higher, prior to the SO corrections detailed in the ESI†. After SO corrections, the ^{5}I state was determined to be the ground state with the ^{5}H only 0.003 eV higher. At the PBE0 and CCSD(T,full) levels of theory, the ^{5}H state lies 0.07 – 0.29 eV above ^{5}I state after SO corrections. The orbitals of the ^{5}I state are shown in Fig. 9 and are similar to those of PrO^+ except the bonding orbitals are no longer filled, decreasing the bond order to two. Other low-lying quintet states were located including $^5\Phi$ ($[\sigma^1\delta^1]\ \sigma^1\pi^3$) and $^5\Pi$ ($[\delta^2]\ \sigma^1\pi^3$), which lie 0.37 – 0.57 and 0.43 – 0.62 eV above the ground state, respectively. Additionally, two septet states, ^{7}H ($[\sigma^1\delta^1\phi^1]\ \sigma^1\pi^2$) and $^7\Sigma$ ($[\sigma^1\delta^2]\ \sigma^1\pi^2$), were also explored and lie 0.04 – 1.09 eV and 0.73 – 1.39 eV above the ground state, respectively.

For PrO_2^+, the molecule is predicted to be linear with a $^3\Phi$ ($[\sigma_u^1\phi_g^1]\ \sigma_g^2\pi_u^4\pi_g^4$) ground state. With z defined as the symmetry axis, the Pr^+ $5d_{z2}$ orbital interacts with the two O $2p_z$ orbitals to form the σ_g bonding molecular orbital (MO) shown in Fig. 9. The bonding π_g orbitals result from the combination of the in-phase Pr^+ $5d_{xz}$ and $5d_{yz}$ orbitals on Pr^+ with the out-of-phase $2p_x$ and $2p_y$ orbitals on the two O atoms. Additionally, the combination of the in-phase $2p_x$ and $2p_y$ orbitals with a small amount of 4f character on Pr^+ gives some bonding character to the ordinarily non-bonding π_u orbitals. Lastly, the remaining two valence electrons are non-bonding and located in the 4f orbitals of Pr^+. The energies, electronic configurations, bond lengths, and

vibrational frequencies for low-lying excited states of the linear inserted $OPrO^+$ species are summarized in Table S3 (ESI†).

Several nonlinear $OPrO^+$ spices were also explored, with the lowest of these being the $^3B_1$ at the PBE0 and CCSD(T) levels of theory. This state has an OPrO angle of ~ 43°, Pr-O bond lengths of ~1.98 Å, and lies 0.67 – 0.89 eV above the linear $^3\Phi$ ground state. Here, the σ_g orbital of the linear species becomes the a_1 MO, the π_g orbitals become the $1b_1$ and $1a_2$ MOs, and the π_u orbitals become the $2a_1$ and $1b_2$ MOs. Two other nonlinear electronic states, both $^3A_1$, with bond angles of ~43° and ~109° were also located and lie 0.65 – 1.04 eV and 0.65 – 2.10 eV above the linear ground state, respectively.

For $PrCO^+$, the molecule is linear with the ground state predicted to be ^5H ($\pi^4\sigma^2$ [$\sigma^1\delta^1\phi^1$] σ^1). The valence electrons of C and O form similar MOs ($\pi^4\sigma^2$) to those of carbon monoxide, Fig. 9; however, the pair of electrons in the σ orbital of CO donates into the empty $5d_\sigma$ orbital of Pr^+ to form a slightly bonding interaction. This interaction in $PrCO^+$ leads to a C-O bond length of 1.116 (B3LYP) and 1.122 Å (PBE0) (Table S5) compared to free CO, 1.124 and 1.123 Å, respectively, which are comparable to the experimental bond length of 1.128 Å.[92] Additionally, the σ nonbonding MO of $PrCO^+$ corresponds largely to a nonbonding Pr^+ 6s atomic orbital with some $5d_\sigma$ character. Thus, Pr^+ retains its ^5I ($4f^3 6s^1$) ground state configuration. A ^5L ($\pi^4\sigma^2$ [$\sigma^1\delta^1\phi^1$] δ^1) low-lying excited state was also found, in which the 6s electron has been promoted to a Pr^+ 5d atomic orbital. The ^5L state lies 0.48 – 0.75 eV higher in energy than the ^5H state and correlates with the ^5L ($4f^3 5d^1$) state of Pr^+ (promotion energy of 0.565 eV). Other low-lying excited states having $4f^3$ configurations with both triplet and quintet multiplicities were also explored and are detailed in the ESI†.

Theoretical BDEs

Theoretical BDES for PrO^+, PrC^+, and $PrCO^+$ were calculated by taking the difference between the ground state PrX^+ and the sum of Pr^+ and X (X = O, C, and CO). For PrO_2^+, the BDE was calculated by taking the difference between the theoretically calculated ground state

PrO_2^+ and the sum of PrO^+ and O. Theoretical energies for a given state correspond to an average energy over all SO levels for that state, whereas the experimental values measure the difference between the ground state SO level of the reactant and products. Therefore, an empirical SO energy correction is required to obtained more accurate comparisons between the theoretical and experimental BDES,[24, 27, 93-96] as described in detail in the ESI†. The first-order SO energy correction to the calculated PrO^+ (^{3}H) BDE is obtained by applying a SO energy correction of 0.201 eV for PrO^+, 0.280 eV for Pr^+, and 0.010 eV for O, resulting in a decrease in the theoretical BDEs of 0.088 eV. For PrC^+ (^{5}I), PrO_2^+ ($^3\Phi$), and $PrCO^+$ (^{5}H), the theoretical BDEs include SO corrections of 0.241, 0.080, and 0.291 eV, respectively.

Experimental and theoretical SO corrected BDEs for PrO^+, PrC^+, PrO_2^+, and $PrCO^+$ are summarized in Table 2, and a comparison between the various values is shown in Fig. 10. When using the Pr basis sets containing an ECP (ANO and Seg. SDD), the PrO^+ BDE are underestimated at the B3LYP and PBE0 levels of theory, whereas at the CCSD(T, full) level of theory, the BDE is in reasonable agreement with experiment. For PrC^+, PrO_2^+, and $PrCO^+$, good agreement between the experimental and theoretical BDEs is obtained, although B3LYP systematically underestimates all three values with PBE0 performing more accurately. CCSD(T) performs well except for PrC^+, where it overestimates the BDE.

Because the ANO and Seg.SDD basis sets only extend up to g functions on the metal cation, insufficient polarization of the metal 4f orbitals resulting from repulsive interactions between them and the bonding MOs could restrict the accuracy of the calculated BDEs. Thus, additional theoretical calculations were conducted for ground state PrO^+, PrC^+, PrO_2^+, and $PrCO^+$ using all-electron cc-pVXZ-DK3 basis sets for Pr (where X = D, T, and Q), and a complete basis set (CBS) extrapolation was performed, as detailed in the ESI†. For the B3LYP and PBE0 approaches, these basis sets generally perform similarly to those using the ECP, although the B3LYP results are worse at the VQZ and consequently, CBS levels. For the CCSD(T) level, results for PrO^+ and PrO_2^+ vary dramatically with basis set size, although the CBS limit performs well. Overall, the lowest mean absolute deviation (MAD) from experiment is obtained for the PBE0/ANO level with CCSD(T)/ANO nearly as low and PBE0/Seg.SDD, B3LYP/ANO, CCSD(T)/Seg.SDD, CCSD(T)/CBS, and B3LYP/Seg.SDD not far behind.

DISCUSSION

PrO^+, PrC^+, PrO_2^+, and $PrCO^+$ BDEs

The measured BDE for PrO^+ is 7.62 ± 0.09 eV. This value is considerably below those in the literature: 8.23 ± 0.10 eV,[29] 8.20 ± 0.16 eV,[40] 8.31 eV,[4] 8.20 ± 0.30 eV,[41] or the best value determined above of 8.27 ± 0.20 eV. In all cases, this can be attributed to the use of IE(PrO) = 4.9 ± 0.10 eV from Ackermann, Rauh, and Thorn.[29] If we combine our value for $D_0(PrO^+)$ with that for $D_0(PrO)$ = 7.70 ± 0.17 eV[38] and IE(Pr) = 5.4702 eV, we obtain IE(PrO) = 5.55 ± 0.19 eV. This higher value is consistent with a discrepancy associated with ionization of molecules at high temperatures. The magnitude of the discrepancy is similar to that found for other metal oxides as well.[7, 10, 23, 28]

The strong bond measured for PrO^+ is consistent with the triple bond formed between the Pr cation and O, as shown in Fig. 9. Gibson has previously shown that the strength of lanthanide oxide cations bond inversely correlates with the promotion energy (E_p) needed to achieve a $5d^2$ electronic configuration on the lanthanide metal that can then form the triple bond with the four

2p electrons on O.[97] The promotion energy needed to achieve the $4f^25d^2$ configuration in Pr is 0.726 eV, obtained from the experimentally measured excitation energy to the Pr^+ ($^5L_6$, $4f^25d^2$) state from the ($^5I_4$, $4f^36s^1$) ground level.[13] As noted in the introduction, kinetic energy dependent product ion cross sections for the reactions of the lanthanide cations Nd^+, Sm^+, and Gd^+ with O_2 using GIBMS have previously been studied.[7, 8, 10] Nd^+ ($4f^46s^1$) and Sm^+ ($4f^66s^1$) are similar to Pr^+ in that they all have ground states of $4f^n6s^1$. In order to achieve a $4f^{n-1}5d^2$ configuration it requires promotion energies of 1.20 and 2.67 eV (although these excited states of Sm^+ are not well characterized).[13] These higher promotion energies correlate reasonably well with the weaker bond strengths of NdO^+ (7.28 ± 0.10 eV) and SmO^+ (5.72_5 ± 0.07 eV) compared to that of PrO^+. In contrast, the ground state of Gd^+ ($4f^75d^16s^1$) already has one 5d electron such that it only requires the excitation of the 6s orbital to a 5d orbital to effectively interact with the four 2p electrons of O. This promotion energy is 0.55 eV,[13] which results in a GdO^+ BDE of 7.69 ± 0.10 eV, slighter stronger than that of PrO^+. Indeed, the average value of $D_0(LnO^+) + E_p(Ln^+)$ equals 8.37 ± 0.10 eV, showing a reasonable correlation.

The BDE for PrC^+ measured here is 2.97 ± 0.10 eV. This BDE is significantly weaker than that that of PrO^+, which is consistent with the bond order of two suggested by the ^5I ground state theoretically calculated (Fig. 9). However, rather than being two-thirds of the PrO^+ BDE, the PrC^+ BDE is 0.44 times that of PrO^+ (after correcting both for the promotion energy). This ratio is similar to that found for NdC^+/NdO^+ and GdC^+/GdO^+ (both 0.45).[8, 10] As the only difference between these species is the occupation of the 4f orbitals, the consistency of the relative values seems reasonable and the $D_0(LnC^+) + E_p(Ln^+)$ sum is 3.75 ± 0.06 eV. The weaker interaction than expected from the bond order in LnC^+ can be attributed to the lower electronegativity of C compared to O, which leads to bonding MOs that are higher in energy than those of LnO^+, as shown for example in Fig. 9. Notably, the SmC^+/SmO^+ ratio is 0.58, with $D_0(SmC^+) + E_p(Sm^+) = 4.83 \pm 0.07$ eV,[7] but here the electronic configuration of SmC^+ has not been investigated.

The measured BDE for PrO_2^+ is 2.47 ± 0.11 eV, in good agreement with the estimated literature value of 2.26 ± 1.10 eV. Each PrO bond in PrO_2^+ is expected to have a bond order of 1.5, arising from the $\sigma_g^2\pi_g^4$ configuration of the $^3\Phi$ ground state, as shown in Fig. 9. After correcting for the promotion energy of 0.726 eV, the OPr^+-O BDE is actually 0.38 ± 0.02 times the Pr^+-O BDE. This ratio is similar to those obtained for NdO_2^+/NdO^+, SmO_2^+/SmO^+, and GdO_2^+/GdO^+: 0.39 ± 0.04, 0.45 ± 0.02, and 0.42 ± 0.01, respectively.[7, 8, 10, 78] Here, the weaker bonds of OLn^+-O can probably be attributed to the fact that both oxygens have to share the same three 5d orbitals on the metal when forming the σ_g and π_g bonds, such that the strength of each bond is diluted. Notably, the only difference between the Pr and Nd species is the occupation of the 4f orbitals, such that similar results are expected, whereas the GdO_2^+ ground state is no longer linear.[78] (The geometry of SmO_2^+ has not been investigated theoretically.)

The BDE measured here for $PrCO^+$ is 0.31 ± 0.07 eV. In the $PrCO^+$ species, the CO binds weakly to Pr^+ as an adduct, consistent with this low bond energy. The ground state of $PrCO^+$ was calculated to be ^{5}H, where the interaction between Pr^+ and CO arises from the interaction of σ donation between the CO bonding MO and the $5d_\sigma$ orbital of Pr^+ (Fig. 9). In this configuration, the 6s electron on Pr^+ (^{5}I) remains in this atomic orbital, maintaining its ground state electronic configuration of 4f36s1. This 6s orbital is largely non-bonding MO, but it does have some repulsive interaction with the σ MO of CO, weakening the bond between the Pr cation and CO.

We now consider the endothermic feature in reaction (7), which was determined to have an initial threshold energy of 0.69 ± 0.12 eV. Given $D_0(Pr^+\text{-O})$ = 7.62 ± 0.09 eV and D_0(OC-O) = 5.453 eV, the formation of ground state PrO^+ in reaction (7) is exothermic by 2.17 ± 0.09 eV. The endothermic feature could correspond to the formation of an excited state of PrO^+ lying 0.69 + 2.17 = 2.86 ± 0.15 eV above the ^{3}H. This excitation energy is consistent with that calculated for the lowest energy quintet state (^{5}I) of PrO^+, 2.63 – 3.64 eV above the ^{3}H ground state of PrO^+ (and in good agreement with the PBE0/ANO value of 2.70 eV), Table S2. The second endothermic feature starts at 2.35 ± 0.2 eV, corresponding to an excitation energy of 4.52 ± 0.24 eV, potentially consistent with PrO^+ ($^5\Sigma$), lying 3.67 – 4.51 eV above the ^{3}H ground state. These

states would be formed in reactions where spin is conserved, unlike the formation of the ^{3}H state. Similar high-energy features have also been observed in the reactions of both Nd^+ and Gd^+ with CO_2, where it was also postulated that spin-conservation lead to the efficiency of the high-energy feature.[8, 10] Additionally, in the reaction of Sm^+ + OCS, SmS^+ also exhibits an endothermic high-energy feature with a threshold that correlates with the calculated excitation energy to the lowest state of SmS^+ having the same spin state as the ground state Sm^+ (^{8}F) reactant.[98] Thus, although spin need not be conserved in these heavy metal systems, spin conservation appears to play a role in the efficiencies of these processes.

Pr Chemi-ionization reaction

The PrO^+ BDE measured here (7.62 ± 0.09 eV) can be combined with the well-established IE of Pr (5.4702 eV[12, 13]) to determine the exothermicity of the Pr chemi-ionization reaction through the thermodynamic cycle 2 shown in Fig. 1. This gives an exothermicity of 2.15 ± 0.09 eV, which is substantially lower than the experimental values of 2.98 ± 0.22,[35] 2.73 ± 0.16,[40] 2.80 ± 0.20,[38] 2.84 ± 0.13,[6] and 2.70 ± 0.14 eV,[33] as determined from literature values of $D_0(PrO^+)$. These differences are attributable to the use of IE(PrO) = 4.90 ± 0.10 eV from Ackermann et al.[29] The results here confirm that Pr is a good candidate for creating localized enhanced plasma regions in the ionosphere via reaction (1).

Despite this strong exothermicity, recent studies of the chemi-ionization reaction (1) with Pr find that the reaction proceeds at about half the collision rate.[11] The reasons for this inefficiency were explored with no satisfactory explanation being determined; however, at the time, this reaction was judged to be exothermic by 2.9 ± 0.2 eV, such that the present change in thermochemistry suggests a reevaluation. As before, reaction (1) with Pr conserves electronic angular momentum, but the strong triply-bound PrO molecule correlates with an excited state of Pr having a $6s5d^24f^2$ configuration, rather than the $6s^24f^3$ configuration of the Pr (^{4}I) ground state (Ω = 9/2 ground level). Not all possible spin-orbit levels of Pr having the former configuration are spectroscopically characterized, but the ones that are known include $^6L_{11/2}$ (0.83 eV), $^6L_{13/2}$

(0.95 eV), $^6I_{7/2}$ (0.99 eV), $^6I_{9/2}$ (1.07 eV), and $^6I_{11/2}$ (1.15 eV), all of which have excitation energies smaller than the 2.15 ± 0.09 eV exothermicity. Thus, excitation to these states during the association of Pr and O should be thermodynamically accessible. In addition, when Pr couples with ground state O ($^3P_2$), formation of the Ω = 7/2 ground level of PrO conserves electronic angular momentum with all of these states except $^6L_{13/2}$. Notably, the other ^6L levels (Ω = 21/2, 19/2, 17/2, 15/2) for which the excitation energies are not known, also cannot form the ground level of PrO and still conserve angular momentum, although excited levels of PrO could be formed instead. It is unknown how these various spin-orbit levels might couple with the states that might lead to the ionization and formation of $PrO^+ + e^-$. Thus, as before, no simple explanation for the inefficiency of reaction (1) with Pr is yet available. This need not be surprising as high-level calculations of the Sm + O chemi-ionization process emphasize the importance of spin-orbit coupling in the excited states of SmO with the chemi-ionization product asymptote.[99]

CONCLUSION

The BDEs for PrO^+, PrC^+, PrO_2^+, and $PrCO^+$ were measured from GIBMS experiments to be 7.62 ± 0.09, 2.97 ± 0.10. 2.47 ± 0.11, and 0.31 ± 0.07 eV, respectively. The Pr^+-O BDE is underestimated at the B3LYP and PBE0 level of theory but better agreement is obtained using the CCSD(T) approach. Better agreement is obtained for the BDEs of Pr^+-C, OPr^+-O, and Pr^+-CO. By combining the measured PrO^+ BDE measured here with the well-established ionization energy for Pr, the exothermicity of the Pr chemi-ionization reaction is evaluated to be 2.15 ± 0.09 eV. This makes Pr a potential candidate to be used in the atmospheric chemical release experiments to create localized enhanced plasmas.

ELECTRONIC SUPPLEMENTARY INFORMATION (ESI†)

A description of the empirical spin-orbit energy correction used for the calculated bond energies. Tables providing detailed summaries of the calculated energies for Pr^+, PrO^+, PrC^+, PrO_2^+, and $PrCO^+$ and the bond lengths and frequencies for the diatomic and triatomic species.

ACKNOWLEDGEMENTS

This material is based upon work supported by the Air Force Office of Scientific Research under AFOSR Award No. FA9550-20-1-0329. The authors thank the Center for High Performance Computing at the University of Utah for generous allocation of computer time.

REFERENCES

1. N. S. Shuman, D. E. Hunton and A. A. Viggiano, *Chem. Rev.*, 2015, **115**, 4542-4570.
2. P. A. Bernhardt, C. L. Siefring, S. J. Briczinski, A. Viggiano, R. G. Caton, T. R. Pedersen, J. M. Holmes, S. Ard, N. Shuman and K. M. Groves, *Radio Science*, 2017, **52**, 559-577.
3. R. G. Caton, T. R. Pedersen, K. M. Groves, J. Hines, P. S. Cannon, N. Jackson-Booth, R. T. Parris, J. M. Holmes, Y.-J. Su, E. V. Mishin, P. A. Roddy, A. A. Viggiano, N. S. Shuman, S. G. Ard, P. A. Bernhardt, C. L. Siefring, J. Retterer, E. Kudeki and P. M. Reyes, *Radio Science*, 2017, **52**, 539-558.
4. K. Schofield, *J. Phys. Chem. A*, 2006, **110**, 6938-6947.
5. S. G. Ard, N. S. Shuman, J. O. Martinez, M. T. Brumbach and A. A. Viggiano, *J. Chem. Phys.*, 2015, **143**, 204303.
6. R. J. M. Konings, O. Benes, A. Kovacs, D. Manara, D. Sedmidubsky, L. Gorokhov, V. S. Iorish, V. Yungman, E. Shenyavskaya and E. Osina, *J. Phys. Chem. Ref. Data*, 2014, **43**, 013101.
7. R. M. Cox, J. Kim, P. B. Armentrout, J. Bartlett, R. A. VanGundy, M. C. Heaven, S. G. Ard, J. J. Melko, N. S. Shuman and A. A. Viggiano, *J. Chem. Phys.*, 2015, **142**, 134307.
8. M. Ghiassee, J. Kim and P. B. Armentrout, *J. Chem. Phys.*, 2019, **150**, 144309.
9. T. Jayasekharan, M. A. N. Razvi and G. L. Bhale, *J. Phys. B: At. Mol. Opt. Phys.*, 2000, **33**, 3123-3136.
10. M. Demireva, J. Kim and P. B. Armentrout, *J. Phys. Chem. A*, 2016, **120**, 8550-8563.
11. S. G. Ard, N. S. Shuman, O. Martinez, P. B. Armentrout and A. A. Viggiano, *J. Chem. Phys.*, 2016, **145**, 084302.
12. E. F. Worden, R. W. Solarz, J. A. Paisner and J. G. Conway, *J. Opt. Soc. Am.*, 1978, **68**, 52-61.
13. J. E. Sansonetti and W. C. Martin, *J. Phys. Chem. Ref. Data*, 2005, **34**, 1559-2259.
14. P. B. Armentrout, *J. Am. Soc. Mass Spectrom.*, 2002, **13**, 419-434.
15. P. B. Armentrout, *Int. J. Mass Spectrom.*, 2000, **200**, 219-241.
16. N. Aristov and P. B. Armentrout, *J. Phys. Chem.*, 1986, **90**, 5135-5140.

17. S. K. Loh, E. R. Fisher, L. Lian, R. H. Schultz and P. B. Armentrout, *J. Phys. Chem*, 1989, **93**, 3159-3167.
18. D. E. Clemmer, J. L. Elkind, N. Aristov and P. B. Armentrout, *J. Chem. Phys.*, 1991, **95**, 3387-3393.
19. M. T. Rodgers, B. Walker and P. B. Armentrout, *Int. J. Mass Spectrom.*, 1999, **182-183**, 99-120.
20. E. R. Fisher, J. L. Elkind, D. E. Clemmer, R. Georgiadis, S. K. Loh, N. Aristov, L. S. Sunderlin and P. B. Armentrout, *J. Chem. Phys.*, 1990, **93**, 2676-2691.
21. Y.-M. Chen and P. B. Armentrout, *J. Chem. Phys.*, 1995, **103**, 618-625.
22. M. R. Sievers, Y.-M. Chen and P. B. Armentrout, *J. Chem. Phys.*, 1996, **105**, 6322-6333.
23. C. S. Hinton, M. Citir, M. Manard and P. B. Armentrout, *Int. J. Mass Spectrom.*, 2011, **308**, 265-274.
24. P. B. Armentrout, *J. Chem. Phys.*, 2013, **139**, 084305.
25. X.-G. Zhang and P. B. Armentrout, *J. Phys. Chem. A*, 2003, **107**, 8904-8914.
26. C. S. Hinton, F.-X. Li and P. B. Armentrout, *Int. J. Mass Spectrom.*, 2009, **280**, 226-234.
27. C. S. Hinton, M. Citir and P. B. Armentrout, *Int. J. Mass Spectrom.*, 2013, **354-355**, 87-98.
28. R. M. Cox, M. Citir, P. B. Armentrout, S. R. Battey and K. A. Peterson, *J. Chem. Phys.*, 2016, **144**, 184309.
29. R. J. Ackermann, E. G. Rauh and R. J. Thorn, *J. Chem. Phys.*, 1976, **65**, 1027-1031.
30. E. Murad, *Chem. Phys. Lett.*, 1978, **59**, 359-361.
31. H. G. Staley and J. H. Norman, *Int. J. Mass Spectrom. Ion Physics*, 1969, **2**, 35-43.
32. L. Gladyszewski, *Folia Societatis Scientarium Lublinensis Mater. Phys. Chem.* , 1974, **116**, 93.
33. M. C. R. Cockett, L. Nyulaszi, T. Veszpremi, T. G. Wright and J. M. Dyke, *J. Electron Spectros. Relat. Phenom.*, 1991, **57**, 373-397.
34. P. N. Walsh, D. F. Dever and D. White, *J. Phys. Chem.*, 1961, **65**, 1410-1413.
35. L. L. Ames, P. N. Walsh and D. White, *J. Phys. Chem.*, 1967, **71**, 2707-2718.
36. L. Brewer and G. M. Rosenblatt, in *Adv. High Temp. Chem.*, ed. L. Eyring, Academic, New York, 1969, vol. 2, pp. 1-83.
37. J. A. Fries and E. D. Cater, *Research in High Temperature Physical Chemistry*, University of Iowa, U. S. Atomic Energy Commission, 1969.
38. J. B. Pedley and E. M. Marshall, *J. Phys. Chem. Ref. Data*, 1983, **12**, 967-1031.
39. M. Dulick, E. Murad and R. F. Barrow, *J. Chem. Phys.*, 1986, **85**, 385-390.
40. E. Murad and D. L. Hildenbrand, *J. Chem. Phys.*, 1980, **73**, 4005-4011.
41. H. H. Cornehl, G. Hornung and H. Schwarz, *J. Am. Chem. Soc.*, 1996, **118**, 9960-9965.
42. J. Kordis and K. A. Gingerich, *J. Chem. Phys.*, 1977, **66**, 483-491.
43. S. K. Loh, D. A. Hales, L. Lian and P. B. Armentrout, *J. Chem. Phys.*, 1989, **90**, 5466-5485.
44. R. H. Schultz and P. B. Armentrout, *Int. J. Mass Spectrom. Ion Processes*, 1991, **107**, 29-48.
45. B. L. Kickel and P. B. Armentrout, *J. Am. Chem. Soc.*, 1995, **117**, 4057-4070.
46. Y.-M. Chen, J. L. Elkind and P. B. Armentrout, *J. Phys. Chem.*, 1995, **99**, 10438-10445.
47. M. R. Sievers, Y.-M. Chen, J. L. Elkind and P. B. Armentrout, *J. Phys. Chem.*, 1996, **100**, 54-62.
48. M. Ghiassee, J. Ewigleben and P. B. Armentrout, *J. Chem. Phys.*, 2020, **153**, 144304.

49. K. M. Ervin and P. B. Armentrout, *J. Chem. Phys.*, 1985, **83**, 166-189.
50. D. Gerlich, in *Adv. Chem. Phys.*, eds. C.-Y. Ng and M. Baer, 1992, vol. 82, pp. 1-176.
51. N. R. Daly, *Rev. Sci. Instrum.*, 1960, **31**, 264-267.
52. F. Muntean and P. B. Armentrout, *J. Chem. Phys.*, 2001, **115**, 1213-1228.
53. P. B. Armentrout and J. Simons, *J. Am. Chem. Soc.*, 1992, **114**, 8627-8633.
54. R. D. Johnson III, NIST Computational Chemistry Comparison and Benchmark Database, http://cccbdb.nist.gov/, (accessed April 12, 2018).
55. R. H. Schultz, K. C. Crellin and P. B. Armentrout, *J. Am. Chem. Soc.*, 1991, **113**, 8590-8601.
56. N. F. Dalleska, K. Honma and P. B. Armentrout, *J. Am. Chem. Soc.*, 1993, **115**, 12125-12131.
57. M. T. Rodgers and P. B. Armentrout, *Mass Spectrom. Rev.*, 2000, **19**, 215-247.
58. M. E. Weber, J. L. Elkind and P. B. Armentrout, *J. Chem. Phys.*, 1986, **84**, 1521-1529.
59. M. J. Frisch, G. W. Trucks, H. B. Schlegel, G. E. Scuseria, M. A. Robb, J. R. Cheeseman, G. Scalmani, V. Barone, G. A. Petersson, H. Nakatsuji, X. Li, M. Caricato, A. V. Marenich, J. Bloino, B. G. Janesko, R. Gomperts, B. Mennucci, H. P. Hratchian, J. V. Ortiz, A. F. Izmaylov, J. L. Sonnenberg, D. Williams-Young, F. Ding, F. Lipparini, F. Egidi, J. Goings, B. Peng, A. Petrone, T. Henderson, D. Ranasinghe, V. G. Zakrzewski, J. Gao, N. Rega, G. Zheng, W. Liang, M. Hada, M. Ehara, K. Toyota, R. Fukuda, J. Hasegawa, M. Ishida, T. Nakajima, Y. Honda, O. Kitao, H. Nakai, T. Vreven, K. Throssell, J. J. A. Montgomery, J. E. Peralta, F. Ogliaro, M. J. Bearpark, J. J. Heyd, E. N. Brothers, K. N. Kudin, V. N. Staroverov, T. A. Keith, R. Kobayashi, J. Normand, K. Raghavachari, A. P. Rendell, J. C. Burant, S. S. Iyengar, J. Tomasi, M. Cossi, J. M. Millam, M. Klene, C. Adamo, R. Cammi, J. W. Ochterski, R. L. Martin, K. Morokuma, O. Farkas, J. B. Foresman and D. J. Fox, *Journal*, 2016.
60. A. D. Becke, *J. Chem. Phys.*, 1993, **98**, 5648-5652.
61. C. Lee, W. Yang and R. G. Parr, *Phys. Rev. B*, 1988, **37**, 785-789.
62. C. Adamo and V. Barone, *J. Chem. Phys.*, 1999, **110**, 6158-6170.
63. J. P. Perdew, M. Ernzerhof and K. Burke, *J. Chem. Phys.*, 1996, **105**, 9982-9985.
64. K. Raghavachari, G. W. Trucks, J. A. Pople and M. Head-Gordon, *Chem. Phys. Lett.*, 1989, **157**, 479-483.
65. S. A. Kucharski and R. J. Bartlett, *J. Chem. Phys.*, 1998, **108**, 5243-5254.
66. G. E. Scuseria and T. J. Lee, *J. Chem. Phys.*, 1990, **93**, 5851-5855.
67. U. Bozkaya and H. F. Schaefer, *J. Chem. Phys.*, 2012, **136**, 204114.
68. X. Cao and M. Dolg, *J. Chem. Phys.*, 2001, **115**, 7348-7355.
69. X. Cao and M. Dolg, *J. Molec. Structure: THEOCHEM*, 2002, **581**, 139-147.
70. M. Dolg, H. Stoll and H. Preuss, *J. Chem. Phys.*, 1989, **90**, 1730-1734.
71. M. Douglas and N. M. Kroll, *Ann. Phys. (N. Y.)*, 1974, **82**, 89-155.
72. M. Reiher and A. Wolf, *J. Chem. Phys.*, 2004, **121**, 10945-10956.
73. Q. Lu and K. A. Peterson, *J. Chem. Phys.*, 2016, **145**, 054111.
74. D. Feller, D. A. Dixon and J. B. Nicholas, *J. Phys. Chem. A*, 2000, **104**, 11414-11419.
75. M. K. Kesharwani, B. Brauer and J. M. L. Martin, *J. Phys. Chem. A*, 2015, **119**, 1701-1714.
76. G. Gioumousis and D. P. Stevenson, *J. Chem. Phys.*, 1958, **29**, 294-299.
77. G. K. Koyanagi and D. K. Bohme, *J. Phys. Chem. A*, 2001, **105**, 8964-8968.
78. M. Demireva and P. B. Armentrout, *J. Chem. Phys.*, 2017, **146**, 174302.

79. J. D. Burley, K. M. Ervin and P. B. Armentrout, *International Joural of Mass Spectrometry and Ion Processes*, 1987, **80**, 153-175.
80. P. Cheng, G. K. Koyanagi and D. K. Bohme, *J. Phys. Chem. A*, 2006, **110**, 12832-12838.
81. M. Demireva and P. B. Armentrout, *Top. Catal.*, 2018, **61**, 3-19.
82. M. R. Sievers and P. B. Armentrout, *J. Chem. Phys.*, 1995, **102**, 754-762.
83. M. R. Sievers and P. B. Armentrout, *Int. J. Mass Spectrom.*, 1998, **179-180**, 103-115.
84. M. R. Sievers and P. B. Armentrout, *Int. J. Mass Spectrom.*, 1999, **185-187**, 117-129.
85. C. Rue, P. B. Armentrout, I. Kretzschmar, D. Schröder, J. N. Harvey and H. Schwarz, *J. Chem. Phys.*, 1999, **110**, 7858-7870.
86. B. Ruscic and D. H. Bross, Active Thermochemical Tables (ATcT) values based on ver. 1.122g of the Thermochemical Network, available at ATcT.anl.gov (accessed 4/29/20).
87. E. Goos, A. Burcat and B. Ruscic, *Journal*, 2016.
88. M. R. Sievers and P. B. Armentrout, *Inorg. Chem.*, 1999, **38**, 397-402.
89. P. B. Armentrout and J. L. Beauchamp, *Chem. Phys.*, 1980, **48**, 315-320.
90. J. L. Elkind and P. B. Armentrout, *J. Phys. Chem.*, 1985, **89**, 5626-5636.
91. E. W. Rothe and R. B. Bernstein, *J. Chem. Phys.*, 1959, **31**, 1619-1627.
92. K. P. Huber and G. Herzberg, *Molecular Spectra and Molecular Structure*, Van Nostrand Reinhold, New York, 1979.
93. H. Lefebvre-Brion and R. W. Field, *The Spectra and Dynamics of Diatomic Molecules*, Elsevier, Amsterdam, 2004.
94. M. A. Garcia and M. D. Morse, *J. Chem. Phys.*, 2011, **135**, 114304.
95. P. B. Armentrout and F.-X. Li, *J. Phys. Chem. A*, 2013, **117**, 7754-7766.
96. J. Kim, R. M. Cox and P. B. Armentrout, *J. Chem. Phys.*, 2016, **145**, 194305.
97. J. K. Gibson, *J. Phys. Chem. A*, 2003, **107**, 7891-7899.
98. P. B. Armentrout, R. M. Cox, B. C. Sweeny, S. G. Ard, N. S. Shuman and A. A. Viggiano, *J. Phys. Chem. A*, 2018, **122**, 737-749.
99. J. Paulovic, L. Gagliardi, J. M. Dyke and K. Hirao, *J. Chem. Phys.*, 2004, **120**, 9998-10001.

Table 1 Summary of optimized modeling parameters in eqn (2) obtained by modeling the experimental reaction cross sections.[a]

Reaction	σ_0	n	p	E_D (eV)	E_0 (eV)	D_0 (eV)
$Pr^+ + CO \rightarrow PrO^+ + C$	0.75 ± 0.34	1.6 ± 0.2	3	9.8 ± 0.1	3.60 ±0.12	7.51 ± 0.12
$Pr^+ + CO \rightarrow PrC^+ + O$	0.67 ± 0.30	1.1 ± 0.1	3	11.3 ± 0.1	8.14 ± 0.10	2.97 ± 0.10
$Pr^+ + CO_2 \rightarrow PrCO^+ + O$	0.14 ± 0.01	1.5 ± 0.1	3	6.0 ± 0.1	5.14 ± 0.07	0.31 ± 0.07
$PrO^+ + CO \rightarrow Pr^+ + CO_2$	0.003 ± 0.001	2.2 ± 0.2	11	7.7 ± 0.1	2.21 ± 0.22	7.66 ± 0.22
$PrO^+ + CO \rightarrow Pr^+ + O + CO$	0.14 ± 0.07	1.0 ± 0.1			7.72 ± 0.23	7.72 ± 0.23
$PrO^+ + CO \rightarrow PrO_2^+ + C$	0.10 ± 0.03	1.7 ± 0.1	4	12.8 ± 0.1	8.59 ± 0.13	2.52 ± 0.13
$PrO^+ + O_2 \rightarrow Pr^+ + O + O_2$	0.10 ± 0.04	1.6 ± 0.2			7.73 ± 0.13	7.73 ± 0.13
$PrO^+ + O_2 \rightarrow PrO_2^+ + O$	0.11 ± 0.03	3.2 ± 0.1	4	6.4 ± 0.3	2.78 ± 0.22	2.34 ± 0.22
$PrO^+ + Xe \rightarrow Pr^+ + O + Xe$	0.02 ± 0.01	2.0 ± 0.1			7.58 ± 0.20	7.58 ± 0.20

[a] Uncertainties are one standard deviation.

Table 2 Experimental and theoretical BDEs (eV) for PrO^+, PrC^+, PrO_2^+, and $PrCO^+$ [a]

Level	Basis set	Pr^+-O	Pr^+-C	OPr^+-O	Pr^+-CO	MAD[b]
Experiment		7.62 ± 0.09	2.97 ± 0.10	2.47 ± 0.11	0.31 ± 0.07	
B3LYP	ANO	6.80	2.76	2.36	0.07	0.35
	Seg. SDD	6.84	2.66	2.31	0.07	0.37
	cc-pVDZ-DK3	6.56	2.52	2.78	0.46	0.49
	cc-pVTZ-DK3	6.64	3.00	2.80	0.47	0.38
	cc-pVQZ-DK3	6.49	2.54	2.98	0.73	0.62
	CBS	6.38	2.21	3.10	0.90	0.81
PBE0	ANO	7.01	3.15	2.45	0.13	0.25
	Seg. SDD	6.82	3.15	2.64	0.14	0.33
	cc-pVDZ-DK3	6.78	3.27	2.90	0.47	0.43
	cc-pVTZ-DK3	6.87	3.35	2.95	0.26	0.42
	cc-pVQZ-DK3	6.73	2.84	3.04	0.18	0.43
	CBS	6.63	2.49	3.10	0.13	0.57
CCSD(T)	ANO	7.83	3.73	2.55	0.12	0.31
	Seg. SDD	7.92	3.76	2.61	0.12	0.36
	cc-pVDZ-DK3	8.21	3.74	3.24	0.58	0.60
	cc-pVTZ-DK3	9.24	3.89	3.78	0.56	1.03
	cc-pVQZ-DK3	8.18	3.77	2.89	0.59	0.52
	CBS	7.42	3.69	2.26	0.61	0.36

[a] Calculated BDEs are both spin-orbit and zero-point energy corrected. CCSD(T) results are obtained from single point calculations using PBE0 geometry optimized structures and vibrational frequencies. [b] Mean absolute deviation from experiment.

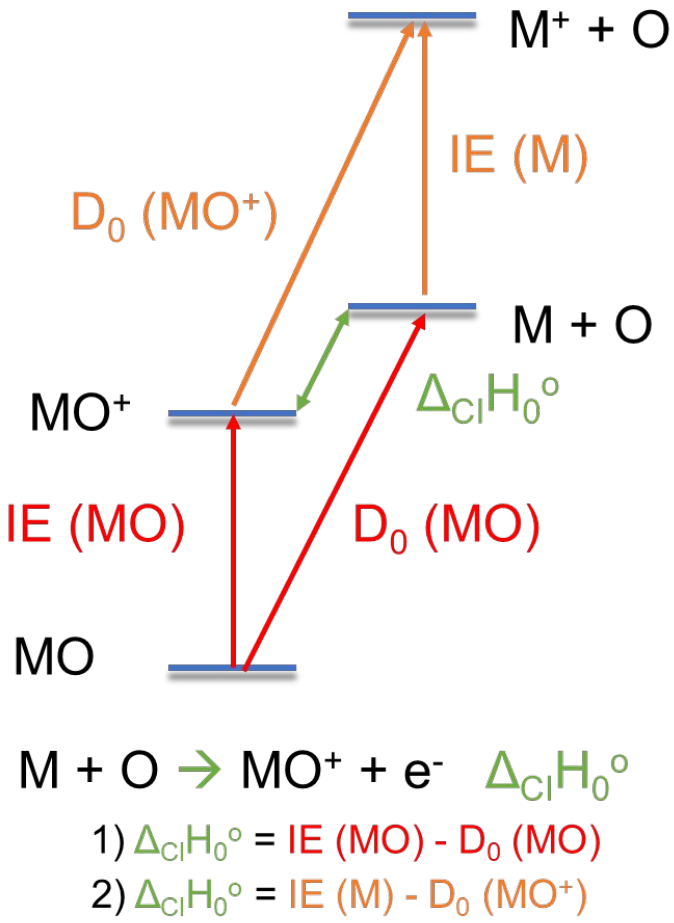

Fig. 1. Thermodynamic cycle that can be used to determine $\Delta_{Cl}H_0^o$ for the chemi-ionization reaction via (1) the ionization energy and bond energy of the metal oxide and (2) the ionization energy of the metal and bond energy of the metal oxide cation.

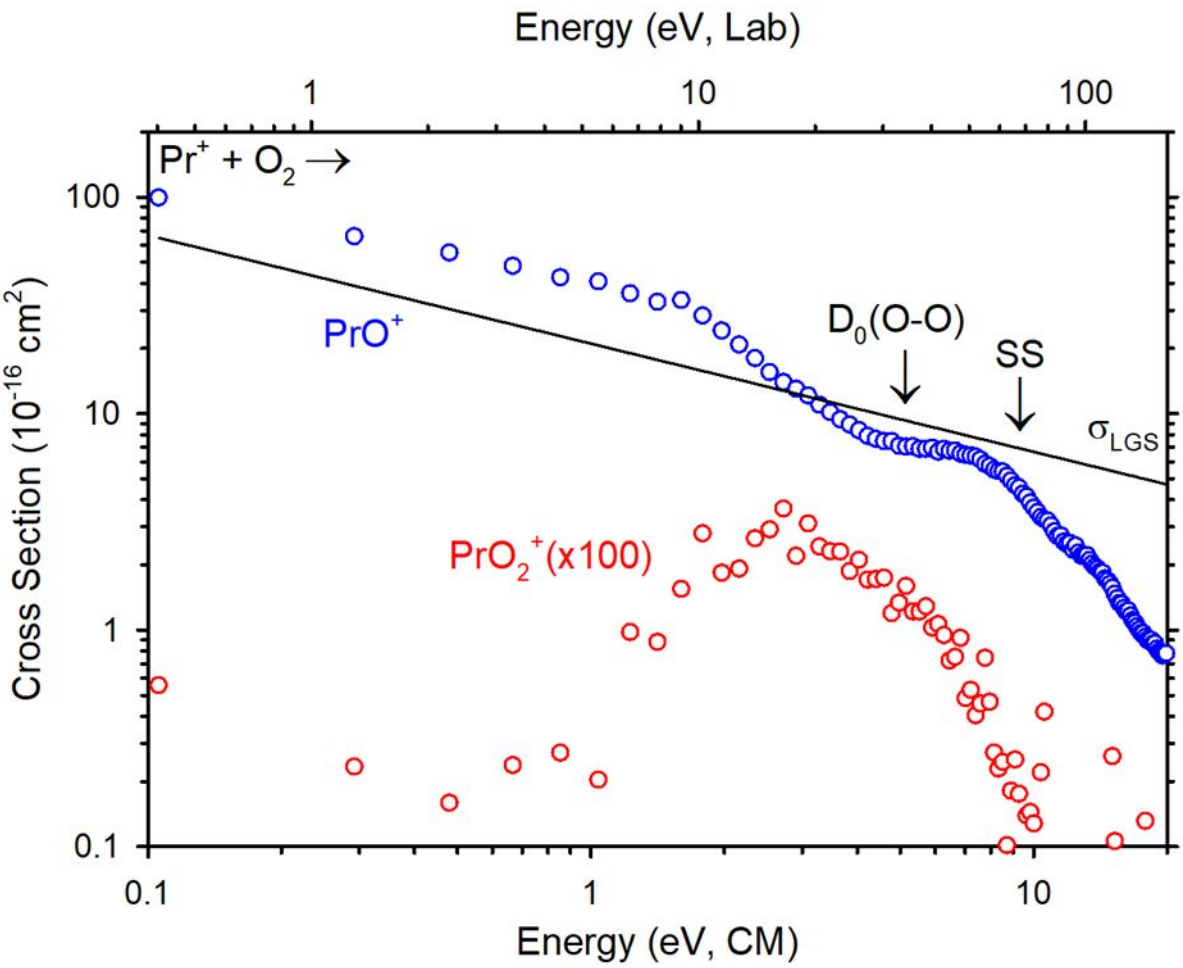

Fig. 2. Product ion cross sections as a function of center-of-mass (lower x-axis) and laboratory (upper x-axis) frame kinetic energy for the reaction between Pr^+ and O_2 (pressure of 0.31 mTorr). The arrows indicate the bond energy of O_2 at 5.12 eV and the spectator stripping (SS) limit for dissociation at 9.3 eV. The solid black line corresponds to the Langevin-Gioumousis-Stevenson collision cross section for this reaction.

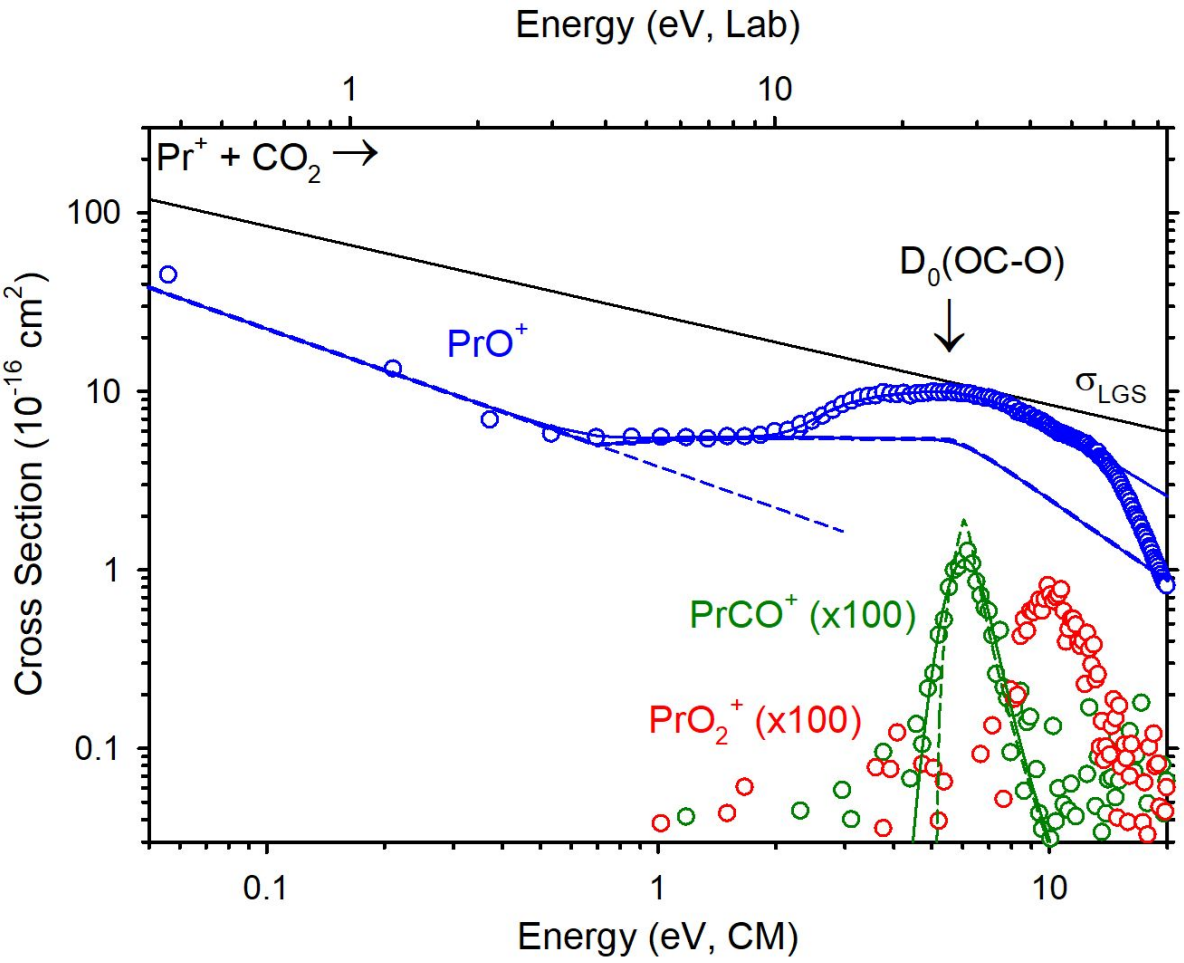

Fig. 3. Product ion cross sections for the reaction of Pr^+ and CO_2 (pressure of 0.30 mTorr) as a function of center-of-mass (lower x-axis) and laboratory (upper x-axis) frame kinetic energy. The arrow indicates the bond energy of OC-O at 5.45 eV. The solid black line is the Langevin-Gioumousis-Stevenson collision cross section for this reaction. Optimized models of the PrO^+ and $PrCO^+$ cross sections using eqn (3) are given by the solid (dashed) green line, which includes (excludes) convolution over the reactant internal and kinetic energy distributions.

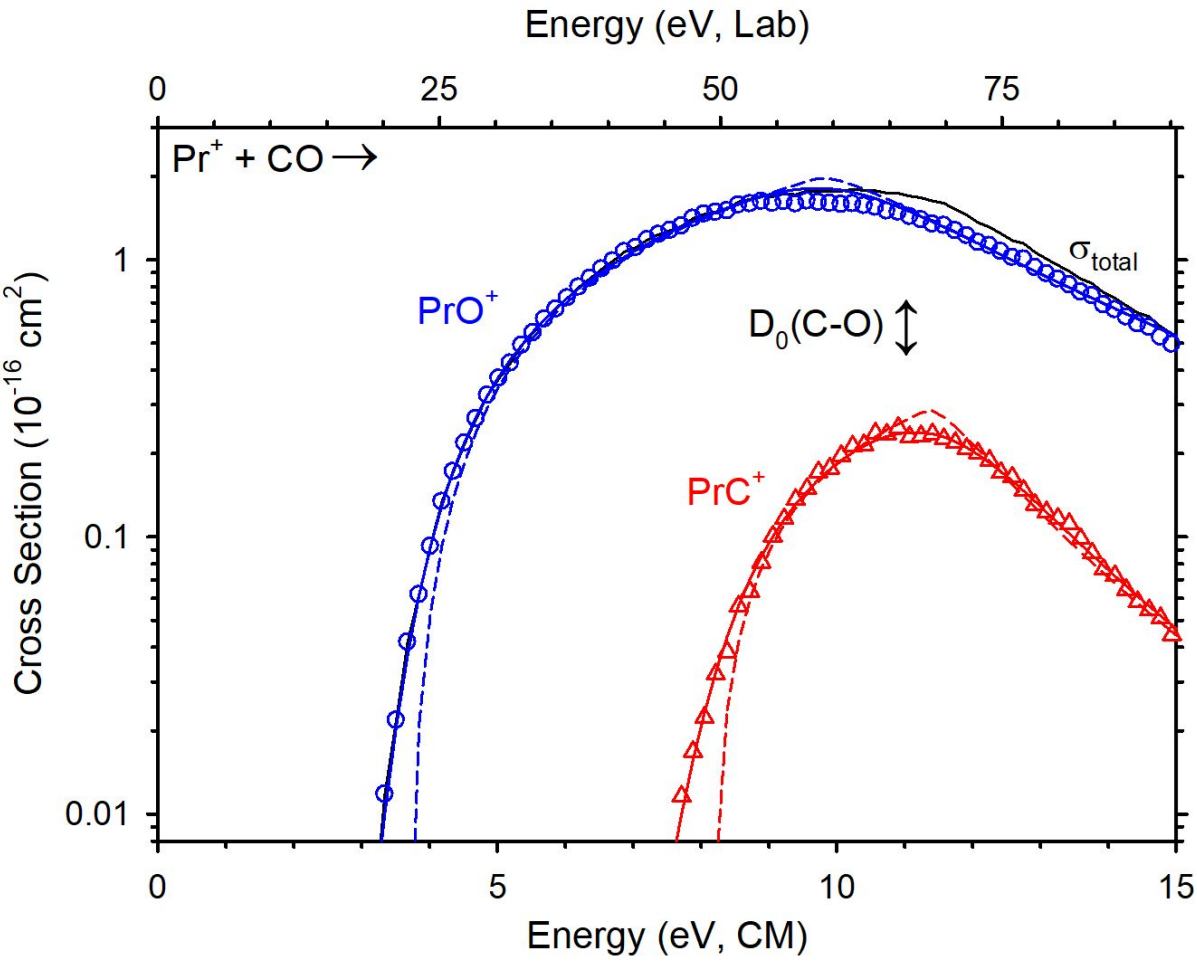

Fig. 4. Product ion cross sections for the reaction between Pr^+ and CO (pressure of 0.31 mTorr) as a function of center-of-mass (lower x-axis) and laboratory (upper x-axis) frame kinetic energy. The arrow indicates the bond energy of C-O at 11.11 eV. The total product ion cross section is given by the solid black line. Optimized models for both cross sections using eqn (3) are given by the solid (dashed) lines, which include (exclude) convolution over the reactant internal and kinetic energy distributions.

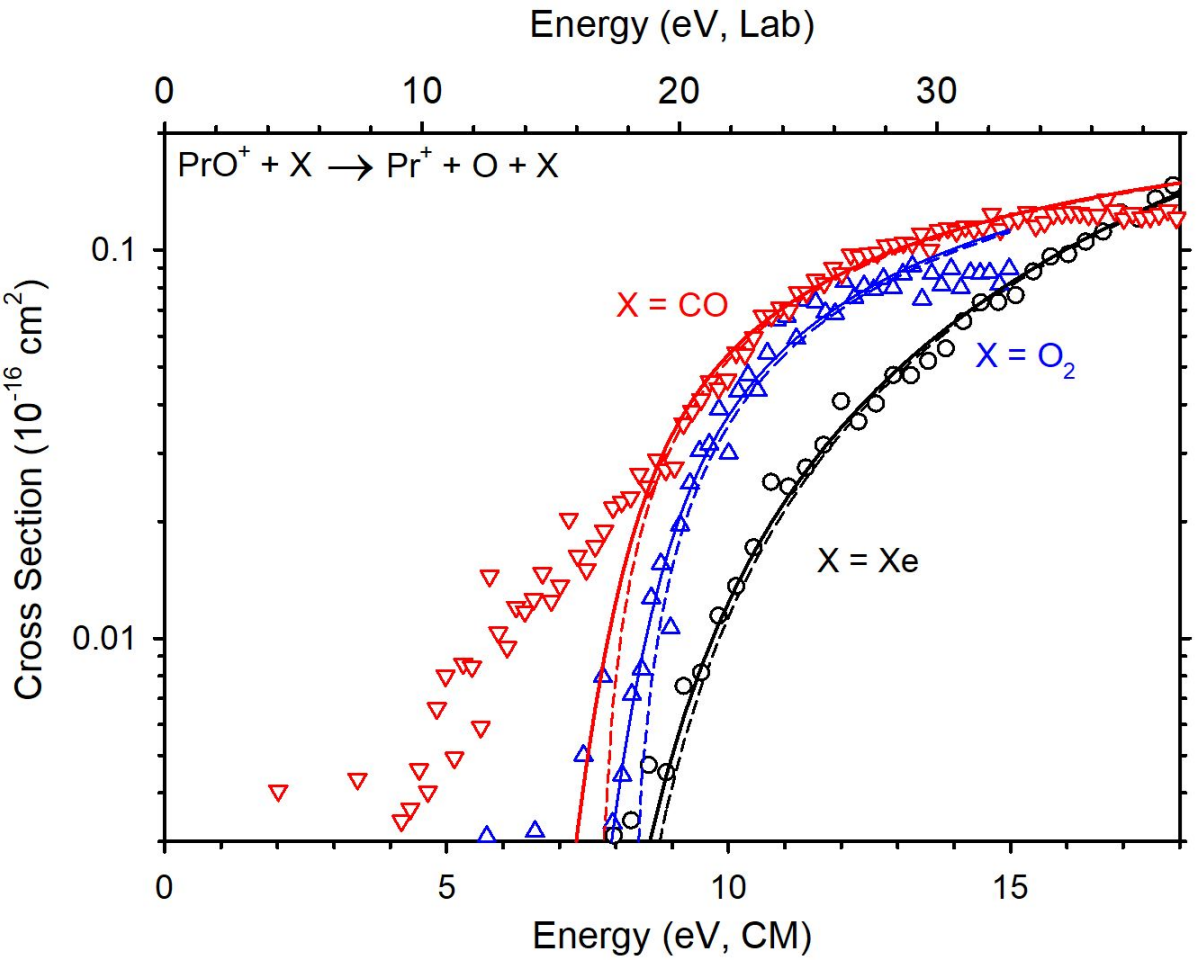

Fig. 5. Comparison of the Pr^+ product ion cross section from the CID reactions of PrO^+ with Xe (black circles, pressure of 0.28 mtorr), O_2 (blue triangles, pressure of 0.30 mTorr) and CO (red inverted triangles, pressure of 0.31 mTorr). The upper x-axis shows the laboratory frame energy scale for the Xe reaction. Optimized fits using eqn (3) are given by the solid (dashed) lines, which include (exclude) convolution over the reactant internal and kinetic energy distributions.

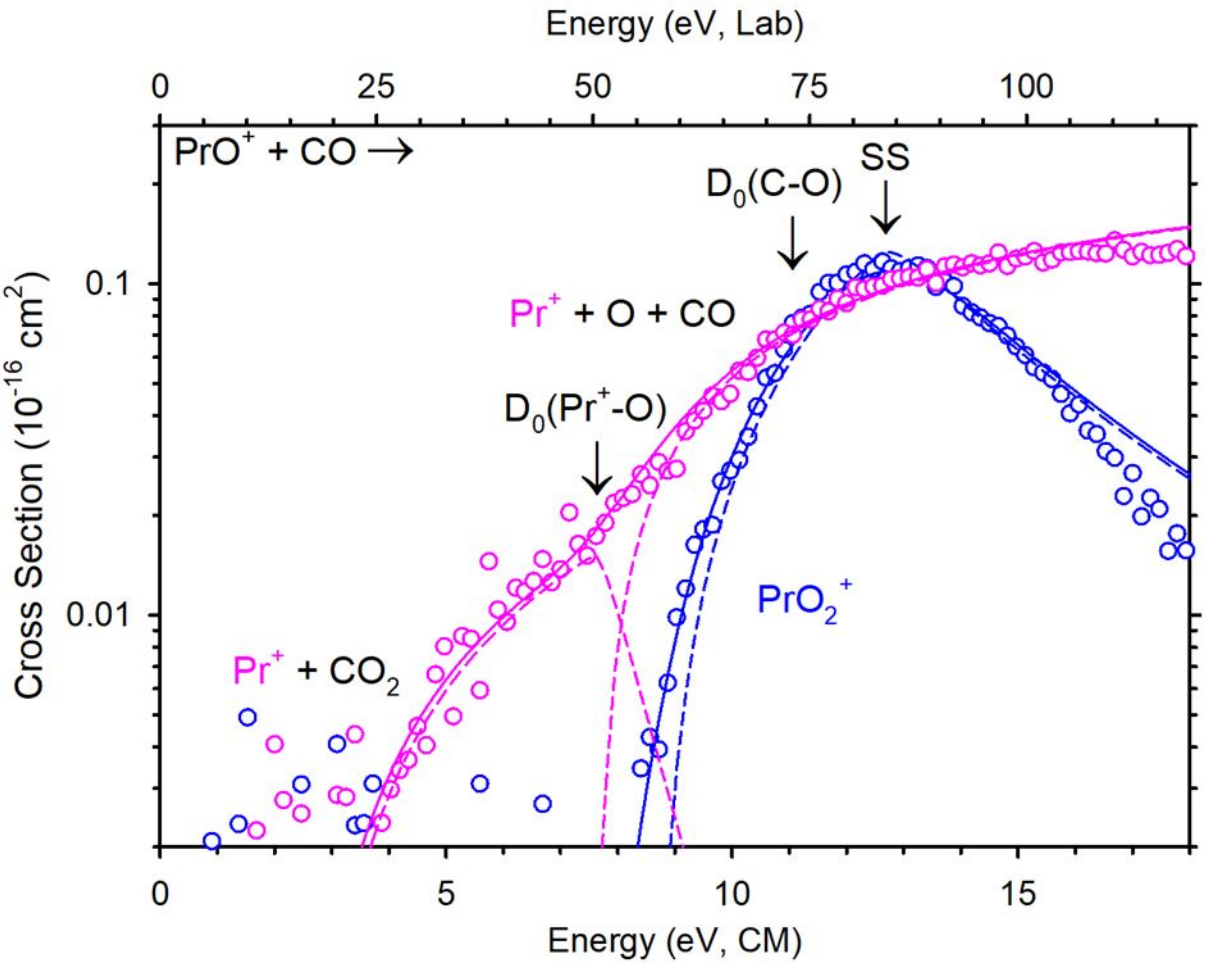

Fig. 6. Product ion cross sections for the reaction of PrO^+ and CO (pressure of 0.31 mTorr) as a function of center-of-mass (lower x-axis) and laboratory (upper x-axis) frame kinetic energy. Arrows indicate the Pr^+-O and C-O bond energies at 7.62 and 11.11 eV, respectively, along with the spectator stripping (SS) dissociation limit at 12.6 eV. Optimized models of the PrO_2^+ cross section and for the low and high energy features of the Pr^+ cross section obtained using eqn (3) are given by the solid (dashed) lines, which include (exclude) convolution over the reactant internal and kinetic energy distributions.

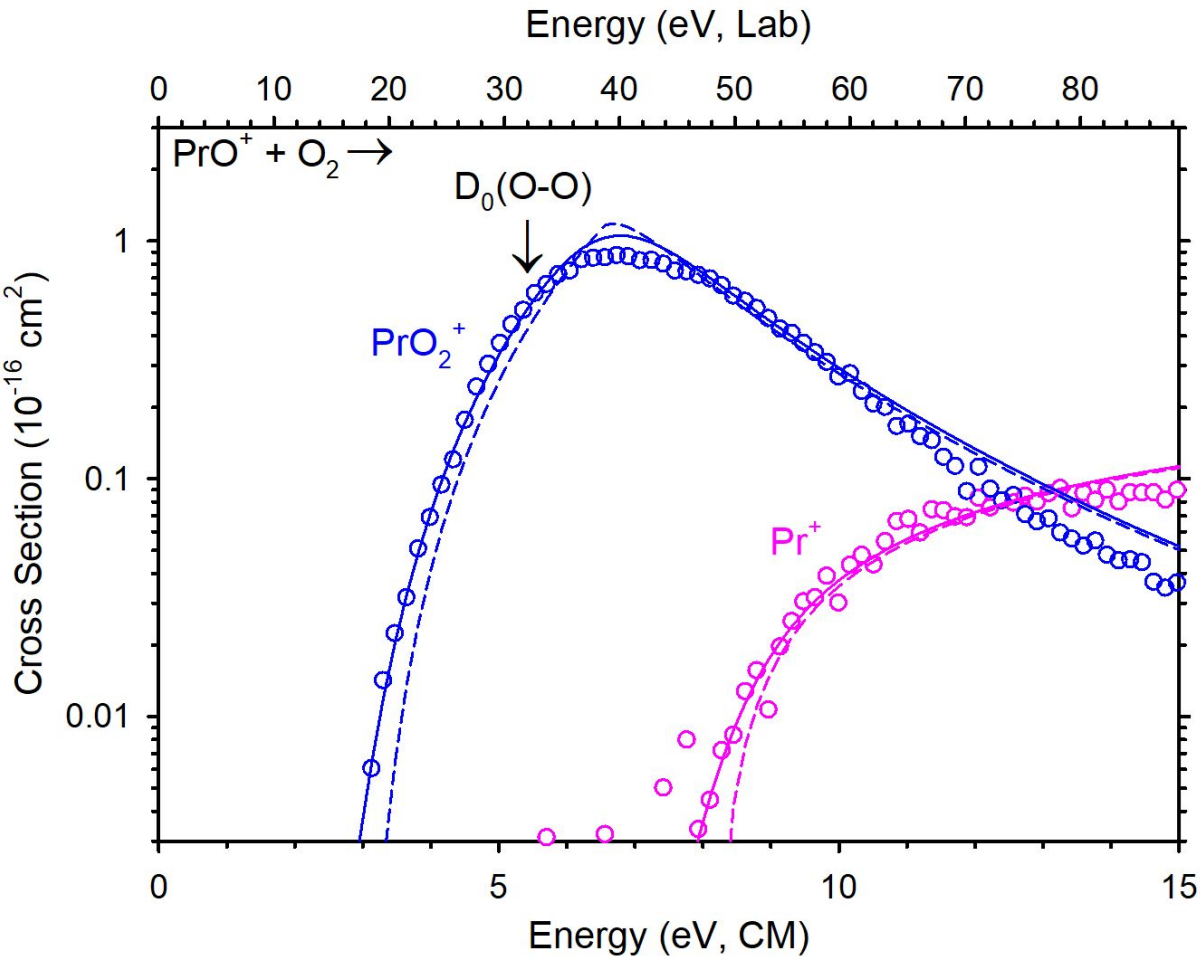

Fig. 7. Product ion cross sections for the reaction of PrO^+ and O_2 (pressure of 0.30 mTorr) as a function of center-of-mass (lower x-axis) and laboratory (upper x-axis) frame kinetic energy. The arrow indicates the bond energy of O_2 at 5.12 eV. Optimized models for both products using eqn (3) are given by the solid (dashed) lines, which include (exclude) convolution over the reactant internal and kinetic energy distributions.

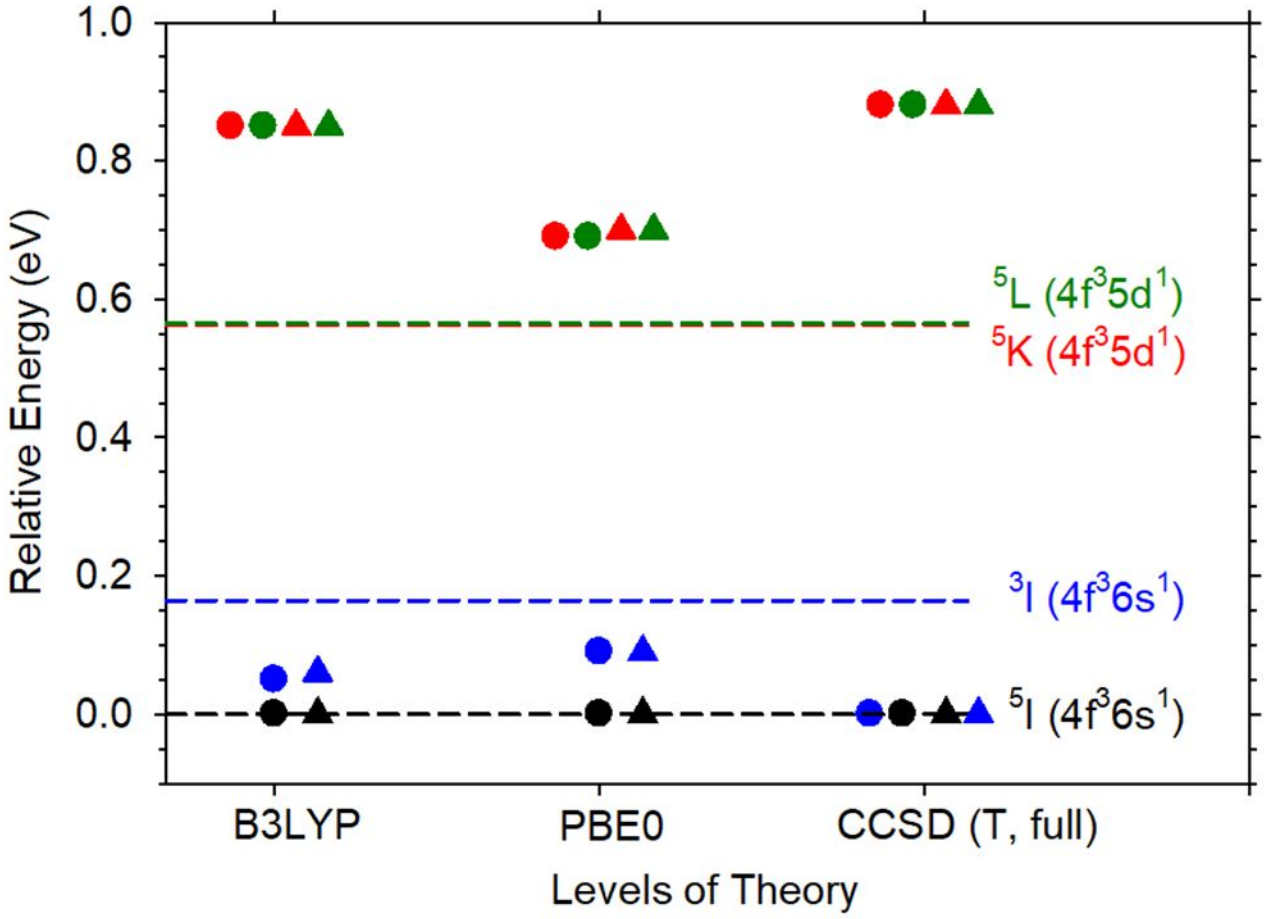

Fig. 8. Comparison between experimental (lines) and calculated (symbols) relative energies for the ground state and several excited states of Pr^+ at the B3LYP, PBE0, and CCSD(T, full) levels of theory using the ANO (circle) and Seg. SDD (triangle) basis sets. Experimental energies are obtained from an average over the SO levels weighted by 2J + 1 (see Table S1).

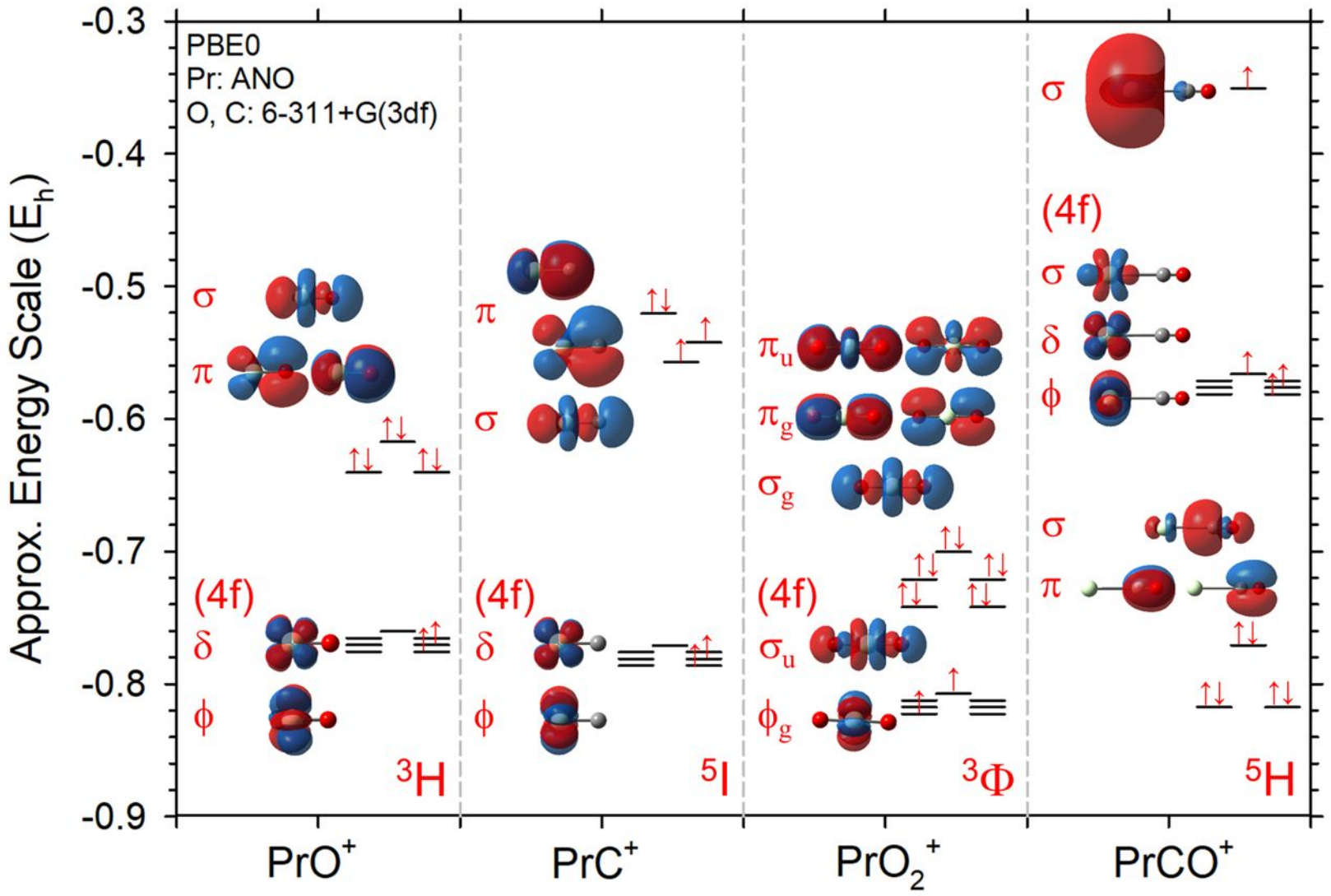

Fig. 9: Molecular orbitals for the ground states of PrO^+, PrC^+, PrO_2^+, and $PrCO^+$ calculated using the PBE0 level of theory and the ANO basis set for Pr.

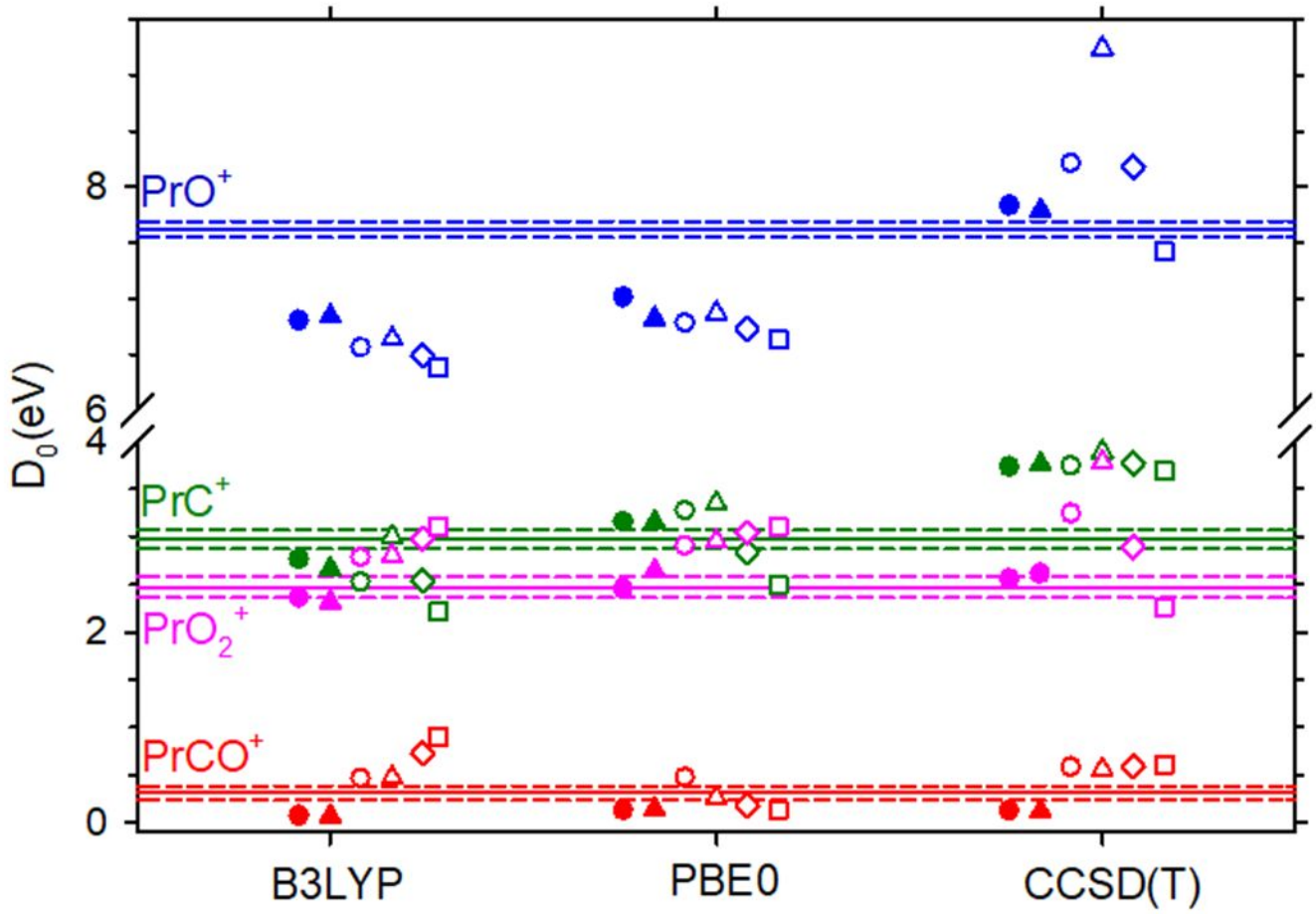

Fig. 10. Comparison between experimental with associated uncertainties (dashed line) and theoretical BDEs for Pr^+-O, Pr^+-C, OPr^+-O, and Pr^+-CO. Theoretical calculations were obtained using the B3LYP, PBE0, and CCSD(T, full) levels of theory using the ANO (filled circles) and Seg. SDD (filled triangles) basis sets for Pr. The $PrCO^+$ BDEs at the CCSD(T, full) level were obtained from single point energy calculations using the PBE0 geometry. Additional calculations for all four molecules using cc-VXZ-DK3 all-electron basis sets are shown for X = D (open circles), T (open triangles), Q (open diamonds), and the complete basis set (CBS) extrapolation (open squares). Theoretical BDEs are SO corrected as explained in detail in the supplementary material.